INORGANIC CHEMISTRY FRONTIERS

RESEARCH ARTICLE

View Article Online
View Journal | View Issue

Cite this: *Inorg. Chem. Front.*, 2026, **13**, 138

Quenching quantum tunnelling of the magnetization utilizing 4d–4f exchange interactions in butterfly-shaped $\{Ru^{III}_2Ln^{III}_2\}$ (Ln = Gd, Tb, Dy, Ho, and Er) single-molecule magnets

Imon J. Dutta,[a] Vignesh Kasi,[b] Deepanshu Chauhan,[b] Keith S. Murray,[c] Stuart K. Langley,[d] Maheswaran Shanmugam *[b] and Kuduva R. Vignesh *[a]

The performance of Single-Molecule Magnets (SMMs) can be enhanced by reducing quantum tunneling of magnetization (QTM), which can be achieved with the aid of strong magnetic exchange interactions and strong magnetic anisotropy. When 4d ions are mixed with 4f ions, the strong spin–orbit coupling and moderate ligand-field strength of 4d elements complement the highly anisotropic 4f ions, and the combined effect decreases the transverse anisotropy and stabilizes the magnetic easy axis, both of which are essential for lowering QTM. Despite their synthetic challenges, the unique electronic properties of 4d–4f systems make them promising candidates for designing advanced single-molecule magnets. Here, we report the synthesis, magnetic, and theoretical studies of five tetranuclear "butterfly-shaped" complexes of formulae $[Ru^{III}_2Ln^{III}_2(OMe)_2(o\text{-tol})_4(mdea)_2(NO_3)_2]$ (Ln = Gd (**1-Gd**), Tb (**2-Tb**), Dy (**3-Dy**), Ho (**4-Ho**), $mdeaH_2$ = *N*-methyldiethanolamine) and $[Ru^{III}_2Er^{III}_2(OMe)_2(o\text{-tol})_6(mdea)_2]\cdot 2MeOH$ (**5-Er**). Complexes **2-Tb**, **4-Ho**, and **5-Er** are the first reported examples of Ru-4f complexes using these Ln^{III} ions. DC magnetic susceptibility studies revealed an antiferromagnetic exchange interaction between the Ln^{III} and Ru^{III} metal ions in all complexes. Among the complexes reported, **3-Dy** and **4-Ho** show out-of-phase susceptibility signals in the absence of an external magnetic field, while the remaining complexes exhibit field-induced slow relaxation of magnetization. These observations were attributed to the presence of an ideal crystal field combined with the strong exchange interaction exerted between the Ru^{III} and Ln^{III} ions in the complexes. Importantly, the **4-Ho** is the first non-dysprosium Ru–Ln polynuclear complex to show zero-field SMM behavior. Detailed *ab initio* CASSCF + RASSI-SO + SINGLE_ANISO + POLY_ANISO and Density Functional Theory (DFT) calculations reveal that the magnitude of exchange interaction increases in the following order: **1-Gd** (–1.3 cm^{-1}) < **2-Tb** (–1.8 cm^{-1}) < **3-Dy** (–2.7 cm^{-1}) < **4-Ho** (–2.8 cm^{-1}) < **5-Er** (–4.0 cm^{-1}). The larger single-ion anisotropy of the Dy^{III} ions in **3-Dy** leads to the largest barrier of 101.8 cm^{-1} (146 K), which increases further to 111 cm^{-1} (158.7 K) when considering the exchange-coupled model, with the strong Ru···Ln exchange further quenching QTM effects. These results highlight the importance of strong magnetic exchange between 4d–4f (Ru^{III}···Ln^{III}) ions in enhancing the SMM behavior of 4d–4f complexes.

Received 6th August 2025,
Accepted 30th September 2025

DOI: 10.1039/d5qi01665g

rsc.li/frontiers-inorganic

Introduction

Single-Molecule Magnets have attracted considerable attention because of their potential use in digital data storage and processing,[1,2] quantum computing,[1,3–5] nanotechnology,[6] and spintronic devices.[7] The main challenges in designing high-performing SMMs are controlling the numerous magnetic relaxation pathways, especially the QTM.[8–10] In order to improve the SMM properties for polynuclear systems, metal ions with a strong anisotropic nature and significant magnetic exchange interaction have become essential.[11] Either a suitable

[a]*Department of Chemical Sciences, Indian Institute of Science Education and Research Mohali, Sector-81, Knowledge City, S.A.S. Nagar, Mohali 140306, Punjab, India. E-mail: vigneshkuduvar@iisermohali.ac.in*
[b]*Department of Chemistry, Indian Institute of Technology Bombay, Powai, Mumbai 400076, Maharashtra, India. E-mail: eswar@chem.iitb.ac.in*
[c]*School of Chemistry, Monash University, Clayton, VIC, Australia 3800*
[d]*Department of Natural Sciences, Chemistry, Manchester Metropolitan University, Manchester, UK*

combination of certain metal ions or the use of radical bridges can significantly increase the magnetic exchange coupling between the metal ions.[12,13] To attain strong magnetic anisotropy, lanthanide (Ln) ions are chosen, which constitute strong unquenched orbital angular momentum compared to 3d transition metals. Some well-known Ln-based SMMs to date include (i) double-decker $Tb(Pc)_2^-$ (Pc = phthalocyanine) with effective energy barriers (U_{eff}) of 330.9 K;[14] (ii) air-sensitive dysprosocenium complexes show U_{eff} more than 2000 K and hysteresis up to 80 K;[15,16] (iii) air-stable Dy(III) single-ion magnets (SIMs) with pseudo-D_{5h} symmetry exhibit a magnetization blocking (T_B) up to 12 K and U_{eff} above 735 K;[17,18] (iv) hexagonal bipyramidal (HBP)-shaped Dy(III)-SIMs with pseudo-D_{6h} symmetry exhibit U_{eff} = 779 K–1360 K;[18–20] (v) mixed-valence dilanthanide complexes of formula $(Cp^{iPr5})_2Ln_2I_3$ exhibit T_B in the range of 28 K–72 K and U_{eff} in the range of 795 K–2345 K.[21,22] At the polynuclear level, the anisotropic properties of Ln ions have also been investigated by incorporating them with 3d metal ions. This strategy revolves around increasing the magnetic exchange interaction (J) between 3d–4f ions to greater magnitudes than possible between 4f–4f ions to reduce the onset of QTM, which is often the cause of fast magnetic relaxation times.[23–26] Thus, larger magnetic exchange interactions are essential for polynuclear systems with long magnetic relaxation timescales. Some of us have reported several $\{Cr_2^{III}Dy_2^{III}\}$ tetranuclear "butterfly" complexes and explored the incremental increase of the energy barrier and blocking temperature (U_{eff} = 31.6 K (22 cm^{-1}) to 93.5 K (65 cm^{-1}) and T_B = 1.8 K to 4.7 K) by modulating the $Cr^{III}\cdots Ln^{III}$ magnetic exchange interaction (−11.2 and −8.3 cm^{-1} to −20.7 and −16.3 cm^{-1}).[27–29] Similarly, we reported an octanuclear $\{Cr_4^{III}Dy_4^{III}\}$ SMM with an energy barrier of 79 K and T_B = 3.5 K, with Cr···Dy magnetic exchange J = −1.8 cm^{-1}.[30] To demonstrate the importance of 3d–4f magnetic exchange interactions in observing SMM behavior, we replaced the Cr^{III} with a diamagnetic Co^{III} ion in both tetranuclear and octanuclear cases, thus removing the exchange interaction. This resulted in a reduced anisotropy barrier for both the butterfly (38 K),[31] and octanuclear complexes (56 K), with a loss of magnetic hysteresis above 1.8 K for all complexes.[32] Many other 3d–4f complexes have been reported with other 3d ions, for example, a $\{Fe_4^{III}Dy_4^{III}\}$ wheel exhibits U_{eff} of 30.5 K with ferromagnetic exchange interaction,[33,34] a 20-nuclearity compound $\{Fe_8Dy_{12}\}$ with an U_{eff} of 3.54 K,[34] a $\{Ni_2^{II}Dy_2^{III}\}$ complex with an anisotropy barrier of 19 K and J_{Ni-Dy} = +0.94 cm^{-1}, a pentanuclear $\{Ni_2^{II}Dy_3^{III}\}$ with U_{eff} of 85 K and T_B = 3 K,[35,36] a $[Mn_4^{III}Ln_4^{III}]$ wheel (Ln = Sm, Gd, Tb, Dy, Ho, Er, and Y) and a $\{Mn_8^{III}Ln_8^{III}\}$ wheel (Ln = Dy, Ho, Er, Y, and Yb) where Mn^{III}–Dy^{III} magnetic exchange is estimated to be −0.1 cm^{-1} and their Dy^{III} analogs are SMMs.[37,38] We believe that these complexes show good SMM behaviour mainly because of their 3d–4f exchange interactions; however, the J values were not determined for some of them either by analyzing DC magnetic data or through computational calculations.

Similar to Ln(III) ions, 4d and 5d metals exhibit stronger spin–orbit coupling (SOC) and larger magnetic anisotropies (highly anisotropic g-tensors with an unusually large ZFS value), leading to slower magnetic relaxation. Among 4d/5d elements, the reported mononuclear SMMs are mostly based on Re^{IV}, Nb^{IV}, $Mo^{III/V}$, Ru^{III}, $W^{III/V}$, and Os^{III} metal ions, which exhibit very large magnetic anisotropy due to their sizeable spin–orbit coupling constant.[39] Among a variety of examples, the complexes involving Re^{IV}, Ru^{III}, Os^{III}, Mo^{III}, and $Nb^{III/IV}$ centers such as $[ReX_4(ox)]^{2-}$ (X = Cl and Br),[40] $[ReCl_4(CN)_2]^{2-}$,[41] *trans*-$[Ru^{III}(salen)(CN)_2]^-$, *trans*-$[Os^{III}(salen)(CN)_2]^-$, fac-$Mo^{III}(Me_3tacn)(CN)_3$, and $[Nb^{III/IV}(CN)_8]^{5-/4-}$, $[Re^{IV}(CN)_7]^{3-}$ are primarily fascinating because they possess large negative ZFS.[42,43] Further to this, a hexanuclear $\{Ru_6^{III}\}$ complex[44] has been shown to exhibit robust magnetic exchange interactions, with J values exceeding −800 cm^{-1}, hence suitable for combining with lanthanide ions to target stronger magnetic exchange interactions compared to 3d–4f complexes. Hence, 4d and 5d ions are preferred compared to their comparable 3d–4f and 4f–4f counterparts, since the more diffuse nature of the 4d/5d orbitals may encourage stronger magnetic exchange and help to reduce QTM and boost SMM performance.[8,45] Thus, despite their synthetic hurdles, 4d/5d–4f systems' unique electronic characteristics will make them interesting candidates for developing improved SMMs. However, there is a paucity of work in this area, with only a handful of polynuclear 4d–4f examples reported in the literature.

One such example is a trinuclear 4d–4f compound $[Co(C_5Me_5)_2][(C_5Me_5)_2Ln(\mu\text{-}S)_2Mo(\mu\text{-}S)_2Ln(C_5Me_5)_2]$, (Ln = Y, Gd, Tb, Dy) reported by Long and co-workers in which the 4d···4f (J_{Gd-Mo}) magnetic exchange interaction is found to be 16.1 cm^{-1}, one of the largest magnetic exchange constants thus far reported with a 4f ion. The Dy^{III} analogue shows slow magnetic relaxation with a U_{eff} = 68 cm^{-1} (98 K), which is the largest reported for a complex containing a paramagnetic 4d metal center.[8] Dunbar group reported CN^--bridged $\{Re_2^{II}Ln_3^{III}\}$ (Ln = Dy and Tb) clusters; however, they are weak SMMs.[46] The two above-mentioned examples are air-sensitive. Similarly, we have shown SMM behavior on a series of air-stable $\{Ru_2^{III}Dy_2^{III}\}$ butterfly complexes, which are the first examples of 4d–4f complexes using the Ru(III) ion.[45,47] The idea of observing strong exchange in 4d–4f complexes is reflected by the findings of this work, which revealed that the exchange interaction was significantly better than any 3d–4f example, except for a $\{Cr_2^{III}Dy_2^{III}\}$ complex.[27] It was shown that the dominant magnetic exchange interaction was observed between the $Ln^{III}\cdots Ru^{III}$ ions varying between −1.9 and −2.42 cm^{-1}. We also showed that by altering the co-ligands, such as the amine polyalcohol and benzoic acid *vs.* acetylacetone, the anisotropy barrier changes, with values ranging from 15.4 K (ref. 45) to 45 K (Scheme 1).[47]

The understanding of what controls the sign and magnitude of the Ru^{III}–Ln^{III} exchange interactions and SMM behavior in these $\{Ru_2^{III}Ln_2^{III}\}$ butterfly complexes needs to be further verified with the development of magneto-structural correlations. Hence, to develop structure–property correlations in these $\{Ru_2^{III}Ln_2^{III}\}$ butterfly complexes, we have expanded the family of complexes by varying substitution in the benzoic acid

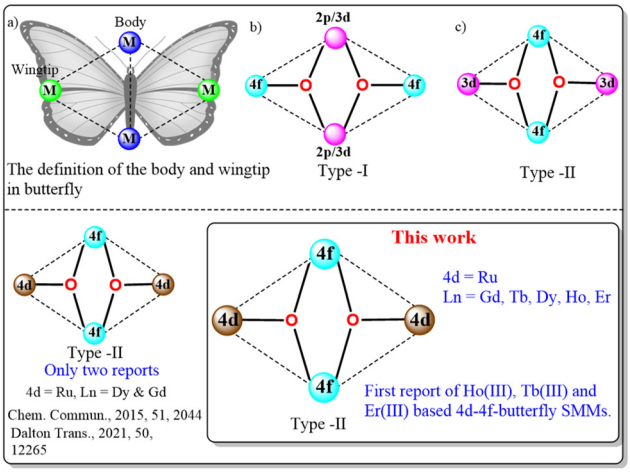

Scheme 1 Schematic representation of a different type of butterfly-shaped 2p/3d/4d–4f SMMs and new 4d–4f SMMs reported in this work.

as well as replacing the anisotropic Dy^{III} ion with other anisotropic Ln^{III} ions such as Tb^{III}, Ho^{III}, and Er^{III}. In this context, we have isolated five $\{Ru_2^{III}Ln_2^{III}\}$ butterfly complexes with the molecular formulae $[Ru_2^{III}Ln_2^{III}(OMe)_2(o\text{-tol})_4(mdea)_2(NO_3)_2]$ (Ln = **1-Gd**, **2-Tb**, **3-Dy**, **4-Ho**) and $[Ru_2^{III}Er_2^{III}(OMe)_2(o\text{-tol})_6(mdea)_2]\cdot 2MeOH$ (**5-Er**) (*o*-tol = *o*-toluate, $(mdea)^{2-}$ = doubly deprotonated *N*-methyldiethanolamine). To the best of our knowledge, complexes **2-Tb**, **4-Ho**, and **5-Er** are the first mixed Ru^{III}-4f SMMs containing anisotropic non-dysprosium ions. Herein, we discuss the synthesis, crystal structure, magnetism, and computational analysis of the $\{Ru_2^{III}Ln_2^{III}\}$ butterfly complexes and explore how the magnetic behaviour is influenced by changing the carboxylate and lanthanide metal ion.

Results and discussion

Syntheses and crystal structures

The reaction of $RuCl_3{\cdot}xH_2O$, $Ln(NO_3)_3{\cdot}xH_2O$ [Ln = Gd, Tb, Dy, Ho, and Er; x = 5 or 6], *ortho*-toluic acid, *N*-methyldiethanolamine ($mdeaH_2$), and triethylamine in acetonitrile solvent generates a dark brown solution.

Subsequent removal of solvent and redissolution of the residue in MeOH gives brown crystals of $[Ru_2^{III}Ln_2^{III}(OMe)_2(o\text{-tol})_4(mdea)_2(NO_3)_2]$ [Ln = Gd (**1-Gd**), Tb (**2-Tb**), Dy (**3-Dy**), and Ho (**4-Ho**)] and $[Ru_2^{III}Er_2^{III}(OMe)_2(o\text{-tol})_6(mdea)_2]$ (**5-Er**) within 2 weeks.

Complexes **3-Dy**, **4-Ho**, and **5-Er** crystallize in the triclinic $P\bar{1}$, space group. For **3-Dy** and **4-Ho**, the asymmetric unit contains half of the complex, *i.e.*, one Ru^{III} and one Dy^{III} metal ion, both of which are positioned on an inversion center. Complex **5-Er** contains two half molecules in the asymmetric unit, which lie upon an inversion centre (Table S1). The tetranuclear complexes $[Ru_2^{III}Ln_2^{III}]$ (Ln = Dy, Ho, and Er) exhibit a butterfly-shaped core structure, where the two lanthanide ions occupy the central body positions and the two Ru^{III} ions are located at the peripheral wing positions (Fig. 1). Each Ln^{III} ion

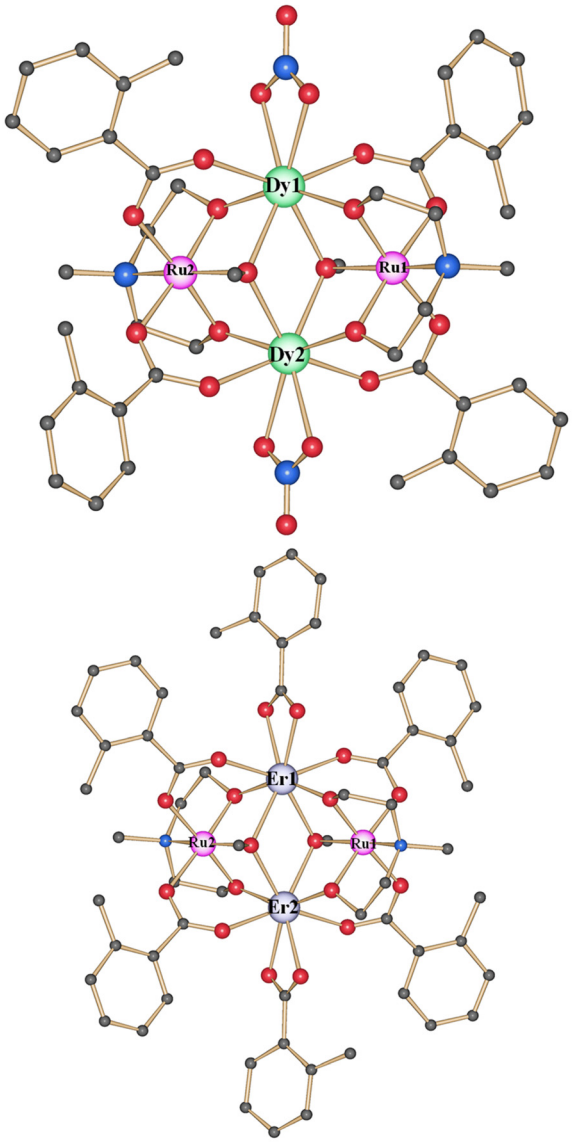

Fig. 1 Molecular structures of complexes **3-Dy** and **5-Er**. The solvent and H atoms are omitted for clarity. Color scheme: Ru^{III}, pink; Dy^{III}, green; Er^{III}, lavender; O, red; N, blue; C, light grey. Complexes **1-Gd**, **2-Tb**, and **4-Ho** are isostructural with **3-Dy**, with the Gd^{III}, Tb^{III}, and Ho^{III} ions replacing the Dy^{III} sites.

is eight-coordinated, surrounded by a combination of oxygen and nitrogen donor atoms from bridging and chelating ligands, resulting in a distorted coordination geometry. The Ru^{III} centers adopt distorted octahedral environments, coordinated by both N and O donor atoms. Two μ_3-methoxide (μ_3-OMe^-) ligands are present, bridging two Ln^{III} ions to a Ru^{III} ion. Furthermore, the complex consists of two $mdea^{2-}$ ligands, which coordinate to one Ru^{III} ion *via* the N-atom, which then bridges from the Ru^{III} to two Ln^{III} ions *via* the two μ_2-O-atoms. Four *o*-toluate ligands are found in complexes **3-Dy** and **4-Ho**, each bridging between a Ru^{III} and a Ln^{III} metal ion. For **5-Er**, six *o*-toluate ligands are present, four again bridge a Ru^{III} and Er^{III} ion, while the final two each chelate to

a single Er^{III} ion. For **3-Dy** and **4-Ho**, the final coordination sites are completed by two nitrate (NO_3^-) ions, which chelate to each Ln^{III} ion. There is no difference in the synthesis method used for **5-Er** compared to those used for the other complexes; the difference in structure may be a consequence of the size of the ion (the smallest of the 4f ions used). The average Ru–O/N bond lengths for **3-Dy**, **4-Ho**, and **5-Er** are found to be 2.036, 2.046, and 2.048 Å, respectively. The average Ln–O bond lengths for **3-Dy**, **4-Ho**, and **5-Er** are found to be 2.369, 2.351, and 2.346 Å, respectively. The Ru^{III} ions of **3-Dy**, **4-Ho**, and **5-Er** possess a six-coordinate octahedral geometry, which, when analyzed by SHAPE analysis, show a CShM of 0.411, 0.400, and 0.399 (Table S2). Similarly, Dy^{III}, Ho^{III}, and Er^{III} metal ions of **3-Dy**, **4-Ho**, and **5-Er** complexes exhibit square antiprismatic geometry with a CShM of 1.747, 1.719, and 1.671 (Table S2).

Single crystals suitable for X-ray diffraction were not obtained for complexes **1-Gd** and **2-Tb**; thus, the solid-state structures of **1-Gd** and **2-Tb** were elucidated through their powder X-ray diffraction (PXRD) patterns (Fig. S1). The experimental PXRD peaks of **1-Gd** and **2-Tb** align closely with the simulated pattern, with all major reflections accurately matched in both position and intensity, showing that these samples possess the same crystal structure as **3-Dy** obtained from SCXRD. Minor discrepancies in relative intensities at lower 2θ, attributable to preferred orientation effects within the powder sample. For **3-Dy**, **4-Ho**, and **5-Er** complexes, sample phase purity is checked by comparing the powder XRD pattern with the simulated single-crystal XRD data (Fig. S1). The core is stabilized by multiple μ-bridging alkoxo or carboxylate ligands, creating a compact and rigid framework that enables short Ru···Ln distances, crucial for effective 4d–4f magnetic exchange interactions. While the overall topology remains consistent across the series, subtle variations in coordination geometry arise from the differing ionic radii and anisotropies of the Dy^{III} and Er^{III} centers, which in turn influence their magnetic behavior and relaxation dynamics.

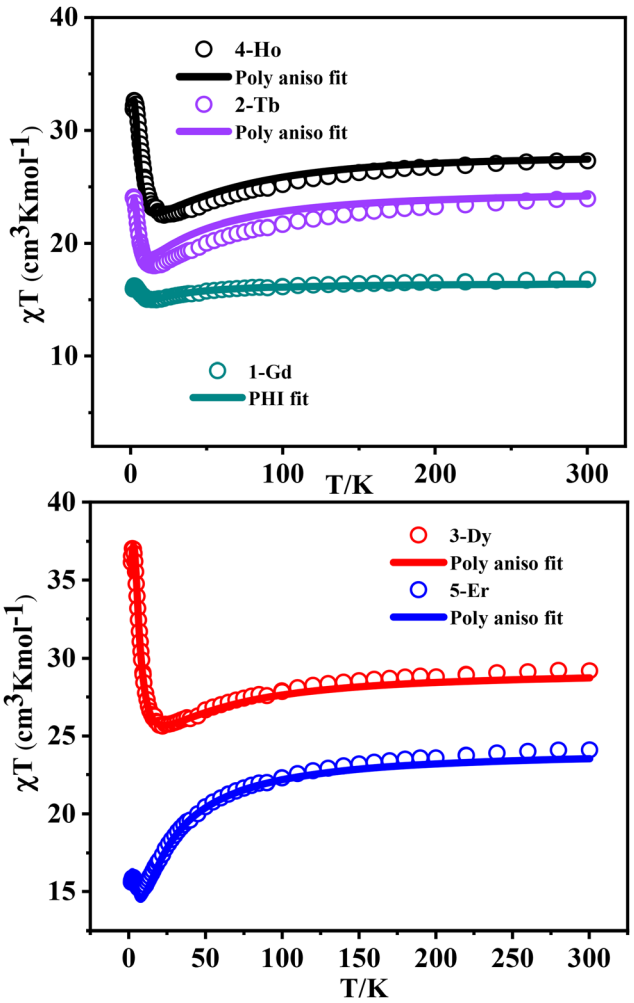

Fig. 2 Experimental χT *vs.* T for complexes **1-Gd**, **2-Tb**, and **4-Ho** (top), **3-Dy**, and **5-Er** (bottom) in an applied magnetic field of 0.1 T. The fitted lines are from the POLY_ANISO[48–50]/PHI program[51] (see below for more details).

Magnetic properties

Direct current magnetic susceptibility measurements. The direct current (DC) magnetic susceptibility measurements on complexes **1-Gd**, **2-Tb**, **3-Dy**, **4-Ho**, and **5-Er** have been conducted across the temperature range of 1.8–300 K in a DC magnetic field of 0.1 T (Fig. 2). The room temperature χT values of **1-Gd**, **2-Tb**, **3-Dy**, **4-Ho**, and **5-Er** are 16.76, 23.90, 29.20, 27.43, and 24.13 cm^3 K mol^{-1}, respectively. These are in good agreement with the calculated values of non-interacting two Gd^{III} (S = 7/2, L = 0, $^8S_{7/2}$, g = 2, C = 7.88 cm^3 K mol^{-1}), two Tb^{III} (S = 3, L = 3, $^7F_6$, g = 3/2, C = 11.82 cm^3 K mol^{-1}), two Dy^{III} (S = 5/2, L = 5, $^6H_{15/2}$, g = 4/3, C = 14.17 cm^3 K mol^{-1}), two Ho^{III} (S = 2, L = 6, $^5I_8$, g = 5/4, C = 14.08 cm^3 K mol^{-1}) ions, two Er^{III} (S = 3/2, L = 6, $^4I_{15/2}$, g = 6/5, C = 11.48 cm^3 K mol^{-1}) ions, and two Ru^{III} (S = 1/2, g = 2, C = 0.37 cm^3 K mol^{-1}) ions of 16.50, 24.39, 29.08, 28.89, and 23.71 cm^3 K mol^{-1}, respectively (Fig. 2).

As the temperature is decreased, the χT product decreases down to 25 K, below which an upturn is observed for all complexes **1-Gd**, **2-Tb**, **3-Dy**, **4-Ho**, and **5-Er**. The high temperature decrease (300–25 K) is due to the depopulation of the excited m_J states of the Ln^{III} ions, while the increase at lower temperatures suggests non-negligible exchange interactions between the Ru^{III} and the Ln^{III} ions (see *ab initio* and DFT analysis). Below 2 K, a sudden drop is observed for all five complexes, due to antiferromagnetic intermolecular interactions (zJ) or dipolar interaction, or the magnetic anisotropy. For **1-Gd**, **2-Tb**, **3-Dy**, **4-Ho**, and **5-Er**, the isothermal magnetization (M) measurements are plotted as a function of the magnetic field (H) and shown in Fig. S2. All the complexes exhibit a sharp rise in magnetization below 2 T, followed by a more steady, linear-like increase that doesn't reach saturation, indicating the presence of low-lying excited states and/or a considerable magnetic anisotropy (Fig. S2). Using the PHI program,[51] the exchange interactions (see Fig. S10) were derived by fitting the dc susceptibility data, which yielded the magnetic exchange constants as follows: $J_{1(Ru–Gd)}$ = −1.0 cm^{-1}, $J_{2(Gd–Gd)}$ =

0.03 cm^{-1}, and $J_{3(Ru-Ru)}$ = −0.07 cm^{-1}. These experimental fitting data suggest that the combination of antiferromagnetic and ferromagnetic interactions within the complex leads to an overall ferrimagnetic behavior.

Alternating current magnetic susceptibility measurements. To study the magnetization dynamics of slow magnetic relaxation, variable temperature and variable frequency AC magnetic susceptibility measurements were carried out. Using a 5 Oe oscillating AC field (0.1–750 Hz) and a zero DC field, complexes **3-Dy** and **4-Ho** showed SMM characteristics. These two complexes show clear frequency-dependent maxima in the out-of-phase (χ''_M) susceptibility component. Over the whole frequency range, peak maxima are found for χ''_M between 1.8–4.5 K and 1.8–3 K for **3-Dy** and **4-Ho**, respectively (Fig. 3).

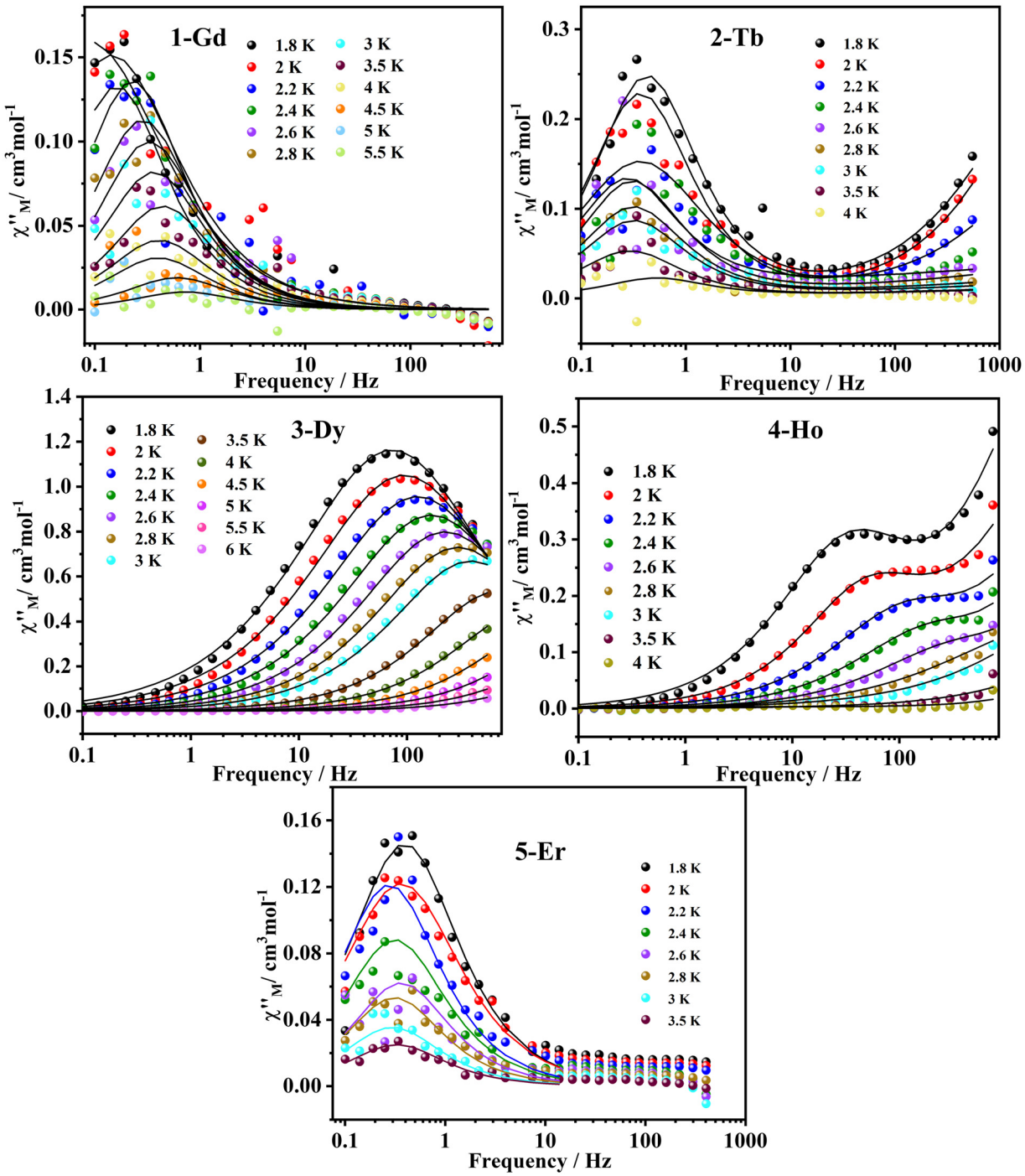

Fig. 3 χ''_M *vs.* frequency plots for **3-Dy** and **4-Ho** (middle-left and middle-right) at H_{dc} = 0 Oe and **1-Gd**, **2-Tb**, and **5-Er** (top-left and top-right and bottom), at H_{dc} = 3600, 2000, and 2400 Oe, respectively. The solid lines are fitted values obtained from the CC-fit[52] program using the parameters given in the text.

Upon application of an optimum external magnetic field of 1600 Oe, **4-Ho** shows clear frequency-dependent maxima in the out-of-phase (χ''_M) signals between 1.8–4 K (Fig. S4) with two relaxations; the maxima at higher frequency are due to QTM, and the maxima at lower frequency were analyzed further. Complexes **2-Tb** and **5-Er** show no out-of-phase (χ''_M) susceptibility peaks in a zero static DC field, but maxima are observed under an applied DC field of 2000 and 2400 Oe, respectively, signifying field-induced SMMs (Fig. 3). This behavior suggests QTM is more significant for **2-Tb** and **5-Er**, which is quenched to some extent under the application of the static DC field. For **1-Gd**, AC measurements performed under a DC field of 3600 Oe revealed maxima in χ''_M *vs.* frequency plot (Fig. 3). Since the Gd^{III} ion is isotropic, the origin of the slow magnetic relaxation for **1-Gd** is attributed to the presence of the anisotropic Ru^{III} ions and the exchange interaction between the Ru^{III} and Gd^{III} ions.

Fig. 3, S5, S6, and S7 are comprised of χ''_M *vs.* frequency, χ'_M *vs.* frequency, and χ''_M *vs.* χ'_M for all five complexes. The Cole-Cole plots of χ''_M *vs.* χ'_M of **1-Gd** and **3-Dy** showed a single semicircular pattern, confirming a single relaxation process, whereas complexes **2-Tb**, **4-Ho** (0 and 1600 Oe), and **5-Er** showed two semicircular patterns, referring to more than one relaxation process (Fig. S6 and S7). The second relaxation process for **2-Tb**, **4-Ho**, and **5-Er** is observed to be largely temperature-independent, suggesting relaxation *via* QTM.[32,62]

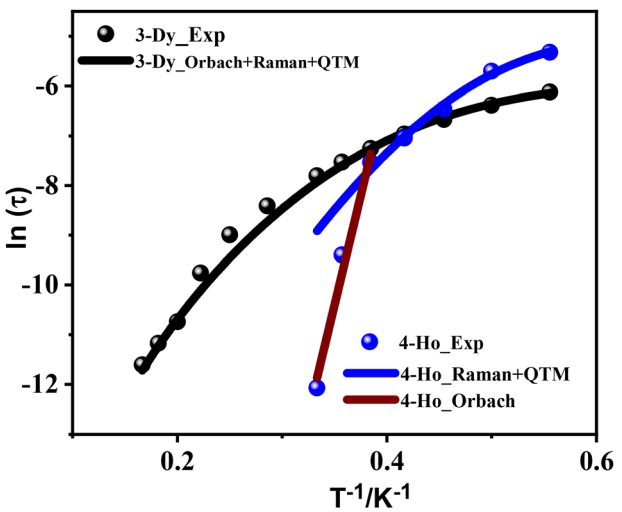

Fig. 4 Magnetization relaxation time (τ), plotted as ln(τ) *versus* T^{-1} for complexes **3-Dy** and **4-Ho**.

Using CC-FIT,[52] the temperature-dependent relaxation data for **1-Gd**, **2-Tb**, **3-Dy**, **4-Ho** (at 0 and 1600 Oe), and **5-Er** were used to extract the relaxation times. The relaxation times (τ) from the CC-FIT,[52] were plotted against 1/T, resulting in a non-linear and Arrhenius plot (Fig. 4, S8, and S9). The best-fit magnetic relaxation parameters are tabulated in Table 1. Fitting the frequency-dependent AC data (solid lines in Fig. 3, S5, S6, and S7) using CC-FIT[52] yields the relaxation times and the associated α parameters (Tables S4–S9). For **3-Dy** and **4-Ho**, the α parameter remains above 0.2 up to 4 K. These higher α values hint at wider distributions that are observed at these temperatures, which are probably a consequence of the interaction of the Raman, QTM, and Orbach relaxation processes. The threshold for **1-Gd**, **2-Tb**, and **5-Er** is 2 or 3.5 K, signifying narrow distributions of relaxation times at higher temperatures, indicating that only the Orbach process is present above 2.5 K and QTM is dominant below that. Eqn (1) was used to fit the data for **3-Dy** and **4-Ho** (0 Oe) by considering all relaxation processes.

$$1/\tau = 1/\tau_{QTM} + CT^n + \tau_0{}^{-1} \exp(U_{eff}/k_BT), \quad (1)$$

where the 1st, 2nd, and 3rd terms correspond to quantum tunneling, Raman relaxation, and Orbach relaxation pathway, respectively. Only fitting the relaxation data to the Arrhenius equation (eqn (2)) was used for **1-Gd**, **2-Tb**, **4-Ho** (1600 Oe), and **5-Er**.

$$\tau = \tau_0 \exp(U_{eff}/k_BT) \quad (2)$$

The non-linear equation fit (eqn (1)) for the ln(τ) *vs.* T^{-1} data yields an energy barrier of 60 K for **3-Dy** and 20 K for **4-Ho** with small QTM values, which supports the observation of zero-field SMM behavior. The QTM is quenched for **4-Ho** upon application of a dc field, which slightly increases the barrier to 22.2 K. Similarly, the QTM is quenched upon application of dc fields for **2-Tb** and **5-Er**, which yield an anisotropy barrier of 30.5 K and 38.9 K, respectively. However, the application of the DC field does not reduce QTM for **1-Gd**, yielding a negligible barrier of 5.5 K. The origin of such a small barrier could be attributed to the anisotropic Ru^{III} ions, considering the isotropic nature of the Gd^{III} ion.

To infer the magnetization blockade, the M *vs.* H hysteresis loops under optimal conditions for all complexes on their polycrystalline samples were measured at 2 K with an average sweep rate of 150 Oe s^{-1}. Unfortunately, no coercivity was

Table 1 Fitting parameters of the relaxation processes for **1-Gd**, **2-Tb**, **3-Dy**, **4-Ho** (at 0 and 1600 Oe), and **5-Er** in the presence and absence of an external DC field

Complex	1-Gd	2-Tb	3-Dy	4-Ho	4-Ho	5-Er
H_{dc}/Oe	3600	2000	0	0	1600	2400
τ_{QTM}/s	1.77	0.00003	0.003	0.008	0.00002	0.4
n			5.64	9		
C/s^{-1} K^{-n}			5	0.4		
τ_0/s	7×10^{-2}	1×10^{-11}	1×10^{-6}	1.5×10^{-11}	9.5×10^{-11}	2.6×10^{-9}
U_{eff}/K	5.5	30.5	60.0	20.0	22.2	38.9

observed in any of the reported complexes, at the temperature and sweep rate measured (Fig. S3 in the SI).

Computational studies

Ab initio and DFT calculations were performed to investigate the observed magnetic properties using MOLCAS 8.2 and Gaussian 16 software, respectively (see Computational details). To investigate the anisotropic nature of individual Ln^{III} and Ru^{III} ions in **2-Tb**, **3-Dy**, **4-Ho**, and **5-Er**, CASSCF/SO-RASSI/SINGLE_ANISO calculations were conducted, followed by the overall magnetic behavior of these complexes, which was rationalized using POLY_ANISO. In all SINGLE_ANISO calculations, the neighboring Ln^{III} and Ru^{III} ions were substituted with diamagnetic Lu^{III} and Y^{III} ions in each of these computations. In POLY_ANISO calculations, the Ru^{III}–Ln^{III}, Ln^{III}–Ln^{III}, and Ru^{III}–Ru^{III} magnetic exchange interactions were computed in order to develop an exchange-coupled states relaxation mechanism for **1-Gd**, **2-Tb**, **3-Dy**, **4-Ho**, and **5-Er**.

Single-ion relaxation mechanism. Tables S10–S12 comprise the energies of low-lying Kramers doublets (KDs)/Ising doublets (IDs) of the individual Ln^{III} and Ru^{III} ions and their respective *g*-tensor values for **2-Tb**, **3-Dy**, **4-Ho**, and **5-Er**. These computed values suggest that both Ln^{III} centers and both Ru^{III} centers are identical to each other in their respective complexes. The ground-state KDs of Dy^{III} ions in **3-Dy**, and IDs of Tb^{III} and Ho^{III} ions in **2-Tb** and **4-Ho** are highly axial, revealing a large g_z value (~19.8 for Dy, ~17.2 for Tb, and ~19.1 for Ho) and negligible transverse components (g_x, g_y), suggesting these Ln^{III} ions are likely to show magnetic relaxation in the excited states. Whereas in **5-Er**, the local *g*-tensors of each Er^{III} ion in the ground KD possess a large transverse component (g_x and g_y), suggesting a high probability of fast QTM.

Fig. 5 displays the orientations of the main anisotropy axes (g_z) in the ground doublets for **2-Tb**, **3-Dy**, **4-Ho**, and **5-Er**. The anisotropic axes of Ln^{III} centers in these complexes are nearly parallel to each other, and the same scenario was observed between the Ru^{III} centers. The local magnetic moments in the ground exchange doublet state of Ru^{III} centers are aligned opposite to the main anisotropy axis of Ln^{III} sites. The Ln^{III} anisotropic axes deviate from the μ_3-O-atoms of methoxides since they possess large LoProp charges of −0.77 to −0.79, which helps them to align in the direction of the O_{meda}–Ln–O_{meda} (O–Ln–O) bond. The parallel alignments between the Dy^{III} ions deviate slightly from the O–Ln–O bond vectors due to the large and differing LoProp charges on the μ_2-O-atoms of $mdea^{2-}$ ligands. In **2-Tb**, **3-Dy**, and **4-Ho**, the anisotropy directions of the Ln···Ln bond vectors lie between the O–Ln–O bond of the $mdea^{2-}$ ligands and the O–Ln–O bond of the *o*-toluate ligands, which can be attributed to the presence of anisotropy directions of the Ru···Ru bond vectors.

The Ln···Ln vectors are tilted by an angle of 30.8°/50.4°, 18.4°/22.3°, and 20.9°/30.7° from the linear O–Ln–O bond vector in **2-Tb**, **3-Dy**, and **4-Ho**, respectively.

Such a small deviation helps to maintain the stronger magnetic anisotropy, which is reflected in their g_z values. Whereas in **5-Er**, the Er···Er bond vectors also lie between the O–Ln–O bond of the $mdea^{2-}$ ligands and the O–Ln–O bond of the *o*-toluate ligands, but closer towards the $O_{o\text{-}tol}$–Er^{III} bonds, and they are tilted by an angle of 89.8°/91.8° from the O–Ln–O bond of the $mdea^{2-}$ ligands, which hints at the presence of weaker anisotropy for the Er^{III} ions.[53,54]

The pronounced tilt of the anisotropy axes in the Er complex originates from the prolate nature of the Er^{III} f-electron density, which favours anisotropy axes oriented perpendicular to the equatorial ligand field. As a result, in **5-Er** the Er···Er vectors are nearly orthogonal (≈90°) to the O–Er–O bond directions of the $mdea^{2-}$ ligands, leading to much weaker axial anisotropy. In contrast, Tb^{III}, Dy^{III}, and Ho^{III} possess oblate electron densities, for which the anisotropy axes preferentially align along the axial O–Ln–O bond vectors, which preserves strong axial anisotropy, consistent with the larger g_z values observed.

To verify the presence of stronger magnetic anisotropies of Tb^{III}, Dy^{III}, and Ho^{III} ions in **2-Tb**, **3-Dy**, and **4-Ho** and the weaker magnetic anisotropy of Er^{III} ions in **5-Er** in their magnetic relaxation pathways, the energy values of eight low-lying Kramers doublets for **3-Dy** and **5-Er**, and the low-lying Ising doublets for **2-Tb** and **4-Ho** were calculated (Table S10). These low-lying doublet states span up to 478.2 cm^{-1}, 551.1 cm^{-1}, 263.2 cm^{-1}, and 338.1 cm^{-1} in **2-Tb**, **3-Dy**, **4-Ho**, and **5-Er**, respectively. The energy gap between the ground and first excited KDs/IDs is found to be 118.3 cm^{-1}, 101.8 cm^{-1}, 70.1 cm^{-1}, and 36.8 cm^{-1} in **2-Tb**, **3-Dy**, **4-Ho**, and **5-Er**, respectively. These low-lying states and the larger gap between each doublet state suggest that **3-Dy** can exhibit the best SMM behavior with a maximum barrier of 551.1 cm^{-1} if QTM is quenched in all the states compared to other analogs.

To corroborate these assumptions, the magnetic relaxation mechanism for each Ln center was developed, and a qualitative explanation of the magnetic relaxation mechanism for each Tb^{III}, Dy^{III}, Ho^{III}, and Er^{III} ion in **2-Tb**, **3-Dy**, **4-Ho**, and **5-Er**, respectively, is illustrated in Fig. 6 and S11. For both the Dy ions (Dy1 and Dy2) in **3-Dy**, QTM is very small in the ground state (0.003 μ_B), which is mainly due to the presence of a highly pure magnetic ground state of m_J = ±15/2, and allows the magnetic relaxation to occur in the excited states. The magnetic relaxation occurs between the first excited state (m_J = ±13/2) as it is highly mixed with other magnetic states m_J = ±11/2, *etc*., leading to significant thermally assisted-QTM (TA-QTM) values (0.24 μ_B) and yielding a barrier of 101.8 cm^{-1} (146 K). This is in reasonable agreement with the experimental U_{eff} value of 60 K. The two Er ions (Er1 and Er2) in **5-Er** possess a significant QTM in the ground state (0.72 μ_B), which is caused by the mixing of the m_J = ±15/2 states with other states such as ±13/2, ±11/2, ±7/2, and ±1/2, *etc*., suggesting magnetic relaxation between the ground KDs itself. The magnetic relaxation is likely to occur in the first excited state if QTM is quenched upon applying a dc field and yields energy barrier of U_{cal} = 36.8 cm^{-1} (52.6 K), which slightly overestimates the experimental U_{eff} value of 38.9 K under a dc field of 2400 Oe.

In the magnetic relaxation diagram of the Tb^{III} ions of **2-Tb**, the ground pseudo-doublet state is a mixture of $m_J = |\pm 6\rangle$ and

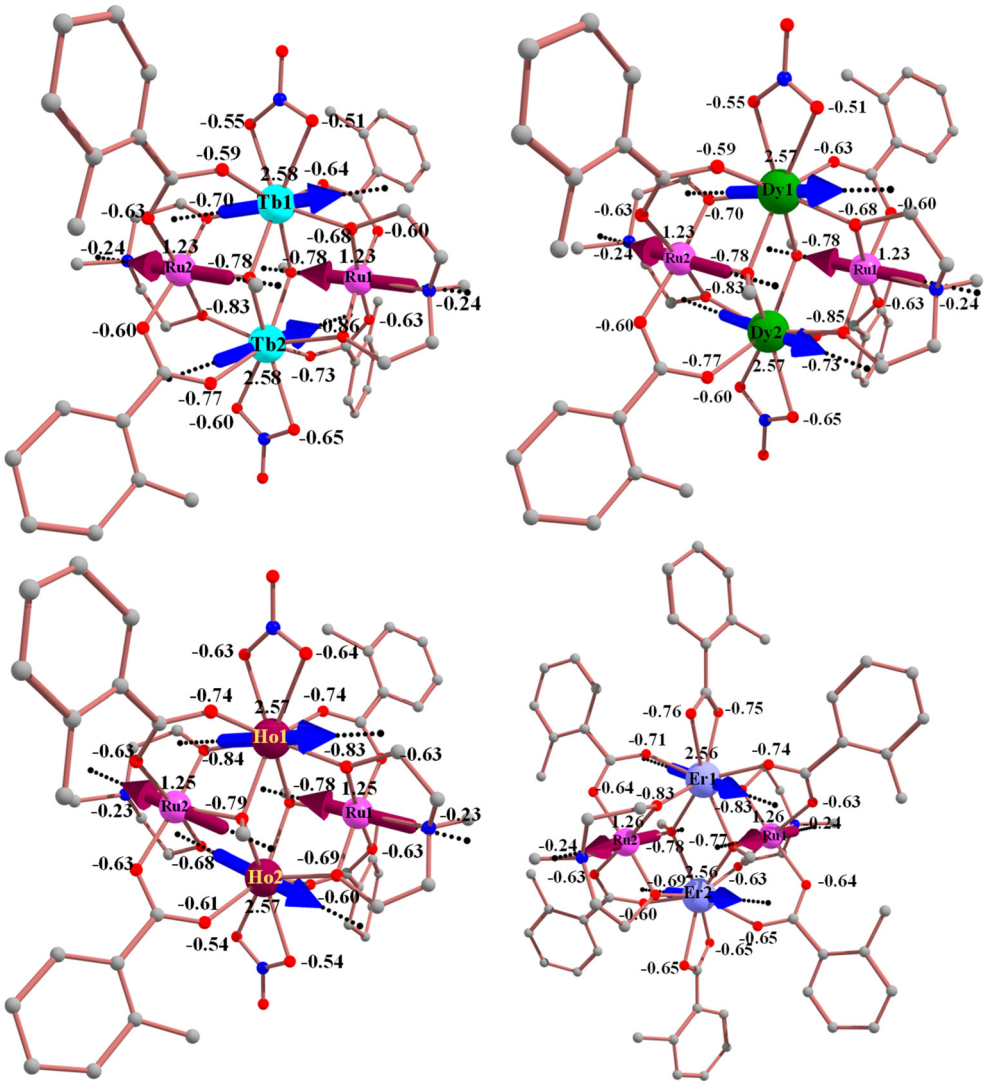

Fig. 5 Magnetic anisotropy directions of complexes **2-Tb** (top, left), **3-Dy** (top, right), **4-Ho** (bottom, left), and **5-Er** (bottom, right), along with the computed LoProp charges on metal and donor atoms. The arrows show the orientation of local magnetic moments in the ground exchange doublet state.

$m_J = |\pm 4\rangle$ states. Due to the highly mixed m_J levels, this results in a non-negligible tunnel splitting of 0.73 cm^{-1}. Hence, strong mixing causes tunneling and quenches the out-of-phase signals at zero dc field. In the case of **4-Ho**, the ground pseudo-doublet state possesses a highly axial g_{zz} value of 19.08, which is closer to the expected value of 20,[55] indicating the strong anisotropic nature of Ho^{III} ions. However, the mixing of the ground $m_J = |\pm 8\rangle$ state with the $m_J = |\pm 4\rangle$ state causes a large tunnelling gap of 1.93 cm^{-1}, and induces QTM. In contrast, slow magnetic relaxation for **4-Ho** occurs in the absence of an applied magnetic field. Therefore, the SMM behaviour of **4-Ho** cannot be accounted for by only considering the single-ion behavior of the Ho^{III} ions. The tunneling gap/QTM could be significantly reduced by applying a DC field, as shown in Fig. S4, or by quenching it with a strong magnetic exchange (Fig. 7).[56,57]

The role of the anisotropic nature of Ru^{III} ions needs to be considered in these complexes, especially for **1-Gd**, where the origin of the SMM behaviour under an applied DC field can be accounted for based on its anisotropic behaviour. The Ru^{III} ions' (t_{2g}^5) unquenched orbital angular momentum is the result of the 4d orbitals' large crystal field splitting and anisotropy. This splitting is a consequence of the strong interaction between the 4d electrons of the Ru^{III} ions and the surrounding ligand field, which significantly alters the energy levels of the d-orbitals, stabilizing the $^2T_{2g}$ configuration as the ground state.[58] The ground-state KDs of the Ru^{III} sites exhibit a rhombic set of *g*-tensors for all four complexes (Table S12); this is anticipated to impact the SMM features, and dominantly in the case of **1-Gd**. The overall magnetic dynamics of these complexes are anticipated to originate from the exchange-coupled state of the entire molecule. According to

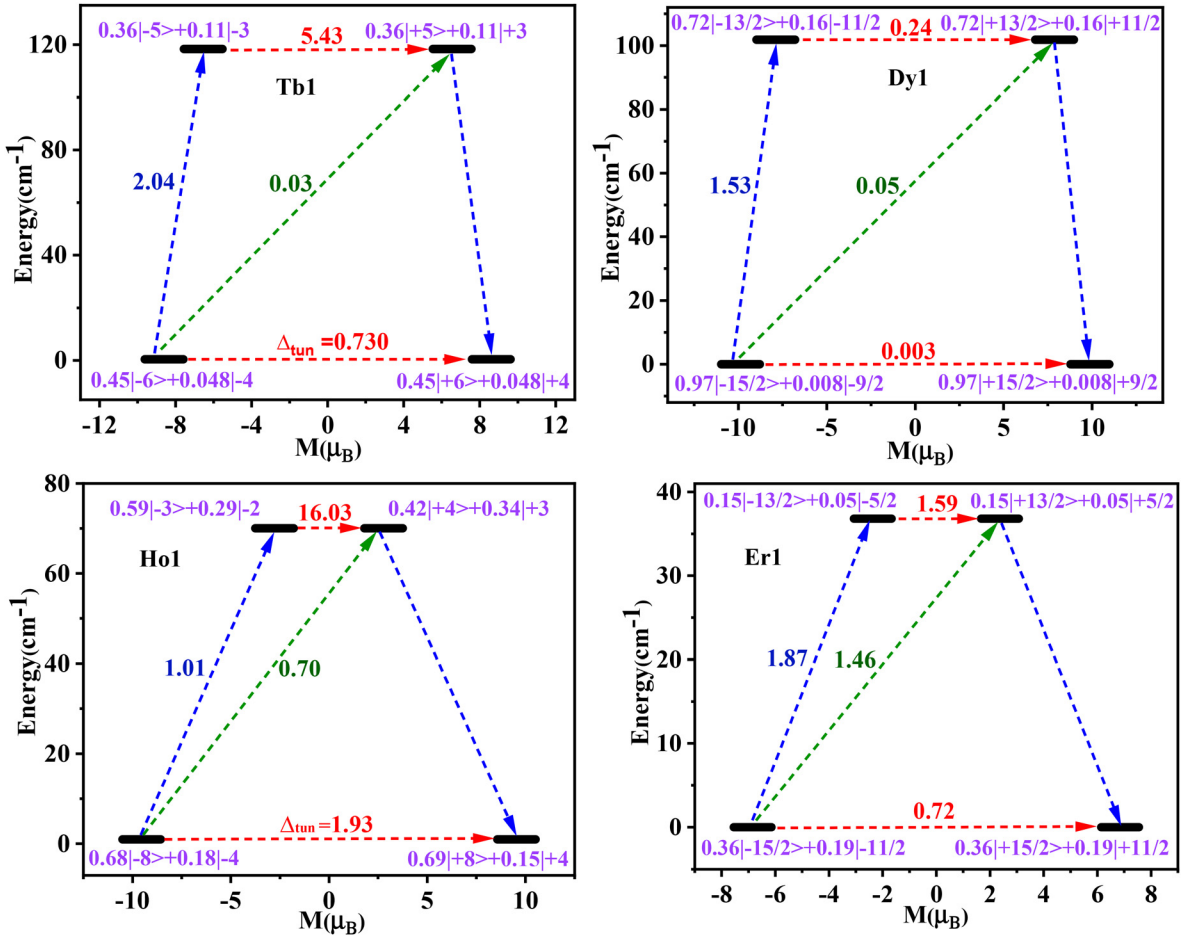

Fig. 6 The *ab initio* computed magnetization blocking barrier for Tb1, Dy1, Ho1, and Er1 ions in **2-Tb**, **3-Dy**, **4-Ho**, and **5-Er**. The thick black line indicates the KDs/IDs as a function of computed magnetic moment. The green/blue arrows show the possible pathway through Orbach/Raman relaxation. The dotted red lines represent the presence of QTM/TA-QTM between the connecting pairs. The numbers provided at each arrow are the mean absolute value for the corresponding matrix element of the transition magnetic moment.

the single-ion viewpoint, complex **3-Dy** should have the best SMM parameters among the five complexes. However, the overall magnetic relaxation will be determined by a combination of the exchange-coupled state and the single-ion behaviour of both Ln^{III} and Ru^{III} ions.

Exchange-coupled states relaxation mechanism

The exchange-coupled states relaxation mechanisms for **1-Gd**, **2-Tb**, **3-Dy**, **4-Ho**, and **5-Er** were developed considering all the possible exchange interactions using the POLY_ANISO program within the Lines model[59] (see Computational details) and by fitting the experimental magnetic data. There are three types of magnetic exchange interactions for each complex: (i) four $J_{1(Ru\cdots Ln)}$ exchange interactions (Ln1–Ru1, Ln1–Ru2, Ln2–Ru1, and Ln2–Ru2), (ii) one $J_{2(Ln\cdots Ln)}$ exchange interaction, and (iii) one $J_{3(Ru\cdots Ru)}$ exchange coupling, as shown in Fig. S10. The calculated J values are tabulated in Table 2. All five complexes possess moderate antiferromagnetic $J_{1(Ru-Ln)}$ interactions and nearly identical and weak ferromagnetic $J_{2(Ln-Ln)}$ exchange interactions. Antiferromagnetic exchange couplings exist between Ru···Ru metal ions for all complexes, where **1-Gd**, **2-Tb**, **3-Dy** and **4-Ho** have similar values (~−0.05 cm^{-1}); however, **5-Er** has the largest (−0.16 cm^{-1}). The intermolecular exchange interaction is found to be antiferromagnetic for all five complexes, which accounts for the decrease in $\chi_M T$ at the lowest temperatures.

To verify the POLY_ANISO computed exchange interactions between the metal centers, the DFT calculations were performed by utilizing Noodleman's Broken Symmetry approach[60] in the Gaussian 16 software[61] (See Computational details). Different spin configurations used to calculate the exchange interactions are shown in Table S15. DFT calculations yield antiferromagnetic exchange (J_{AF}) coupling values for $J_{1(Gd-Ru)}$ = −1.32 cm^{-1}, ferromagnetic exchange (J_F) value for $J_{2(Gd-Gd)}$ = ~0.01 cm^{-1}, and antiferromagnetic exchange value of $J_{3(Ru-Ru)}$ = −0.24 cm^{-1}, leading to an S = 6 ground state. These DFT-computed J values are in good agreement with PHI-fitted J values (see Table 2) and also align well with the POLY_ANISO computed J values for other complexes, with slight variation in their magnitudes (see more discussion in SI). Among all the

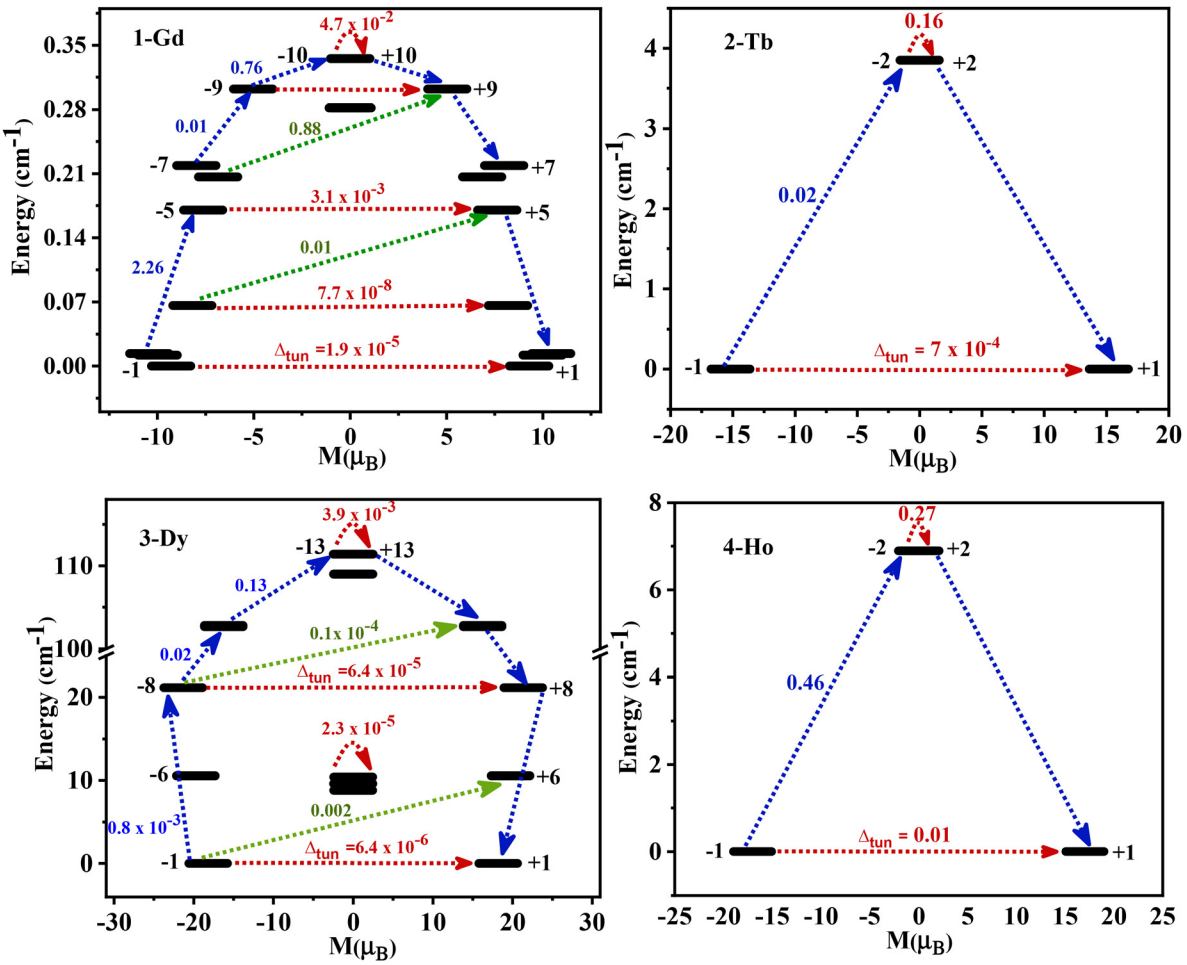

Fig. 7 Low-lying exchange spectra in **1-Gd**, **2-Tb**, **3-Dy**, and **4-Ho**. The exchange states are placed on the diagram according to their magnetic moments (bold black lines). The red arrows show the tunneling transitions (energy splitting) within each doublet state, while the green/blue arrows show the possible pathway through Orbach/Raman relaxation. The numbers on the paths are averaged transition moments in μ_B, connecting the corresponding states.

Table 2 Exchange coupling constants (J; in cm^{-1}) were estimated using POLY_ANISO and DFT calculations for **1-Gd**, **2-Tb**, **3-Dy**, **4-Ho**, and **5-Er**.

		Lines model				
J (cm^{-1})	DFT **1-Gd**	**1-Gd**	**2-Tb**	**3-Dy**	**4-Ho**	**5-Er**
J_1 (Ru–Ln)	−1.32	−0.4	−1.8	−2.7	−2.8	−4.0
J_2 (Ln–Ln)	0.01	0.01	0.03	0.05	0.01	0.01
J_3 (Ru–Ru)	−0.24	−0.05	−0.05	−0.05	−0.05	−0.16
zJ		−0.001	−0.015	−0.014	−0.015	−0.034

complexes, **5-Er** possesses the largest $J_{1(Ru\cdots Ln)}$ exchange interaction, which is a common observation for Er-based complexes, and this can be attributed to the prolate nature of erbium's electron density.[62,63] For **2-Tb**, **3-Dy**, and **4-Ho**, which are oblate-Ln ions, the Ru–O–Ln angle is found to be 99.1°, 99.1°, and 98.9°, respectively, which is in accordance with their oblate nature (Tb ~ Dy > Ho), and their $J_{1(Ru\cdots Ln)}$ values are also in the reverse order of oblate nature. Whereas, the Gd ion is spherical in shape, giving the smallest $J_{1(Ru\cdots Gd)}$ value among all. The overall $J_{1(Ru-Ln)}$ exchange interaction is dominant among all three exchange interactions and follows the trend in the order of complexes **5-Er** > **4-Ho** > **3-Dy** > **2-Tb** > **1-Gd**. This trend, as elucidated above, can therefore be attributed to the gradual transition in the nature of the 4f electron density distribution of the lanthanide ions, which increases when they possess prolate Ln ions and decreases for spherical Gd ions. Furthermore, this can be linked to the combination of J_F and J_{AF}, leading to the overall J value. The number of orbital overlaps is greatest for Ru^{III}–Gd^{III} (one 4d orbital and seven 4f orbitals), with some of these contributing to J_F, reducing the magnitude of the antiferromagnetic $J_{1(Ru-Gd)}$ exchange.[64–67] As we move across the series, the number of magnetic exchange overlaps is reduced (*e.g.*, only three overlaps in Ru–Er, *i.e.*, one 4d orbital and three 4f orbitals, which lowers the J_F part), resulting in the increment of the magnitude of antiferromagnetic $J_{1(Ru-Ln)}$ exchange (**5-Er** > **4-Ho** > **3-Dy** > **2-Tb** > **1-Gd**).

Fig. 7 and S15 show the POLY_ANISO computed exchange-coupled states' mechanism of magnetic relaxation of **1-Gd**,

2-Tb, **3-Dy**, **4-Ho**, and **5-Er** that was developed using all three exchange coupling constants. The two lanthanide metal ions in each complex, possessing ground Kramers/Ising doublet states, coupled with two Ru^{III} ions, yielded a non-Kramers exchange spectrum for all complexes. The lowest exchange doublets from the spectrum with their tunnel splitting, and the g_z value of each doublet are given in Tables S16–20. In the case of **3-Dy**, a very small tunneling gap (~10^{-6} to 10^{-4} cm^{-1}) was observed at the ground state as well as in lower excited states. This gap is enlarging at the 12th excited state, which allows the magnetic relaxation to happen *via* 12th excited exchange states and yields an energy barrier (U_{cal}) of 111 cm^{-1} (158.7 K). This corroborates the observation of SMM behaviour for complex **3-Dy** in the absence of a DC field, but this U_{cal} value is overestimated, and this can be attributed to the exclusion of hyperfine interactions in our calculations.[68,69] Similarly, for complexes **2-Tb** and **4-Ho**, the tunneling gap is small in the ground state, but it becomes larger in the 1st excited state, which allows the magnetic relaxation with a barrier of 3.9 cm^{-1} (5.6 K), and 6.9 cm^{-1} (10 K), respectively. These values suggest that **2-Tb** and **4-Ho** can show SMM behaviour with a small dc field or without a dc field, which is in accordance with the experimental observation, but slightly underestimated. Though comparatively a large tunnelling gap between the ground doublet is predicted at each Ho(III) single-ion for **4-Ho**, resulting in efficient QTM, the Ru–Ho exchange interaction raised the degeneracy and produced a ladder of exchange-coupled states, which in turn helped to reduce the tunnelling gap. Slow magnetic relaxation takes over as a result of the suppression of the tunnelling gap at the ground exchange-doublet states, which supports the observation of the maxima in the AC magnetic susceptibility data at lower temperatures from 1.8–3.5 K in the absence of a dc magnetic field. Thus, the interplay between the large intrinsic tunnelling gap and the exchange-induced level splitting explains why Ho exhibits observable zero-field dynamics despite its unfavorable single-ion characteristics. For **1-Gd**, the ground state, as well as several low-lying excited states, possess a very small tunneling gap (~10^{-8} to 10^{-3} cm^{-1}), but these states are stacked very closely, leading to a negligible energy barrier of 0.3 cm^{-1} (0.4 K). Whereas for **5-Er**, the tunneling gap is large even at the ground state, allowing for relaxation with a negligible energy barrier (U_{cal}). These negligible U_{cal} values of **1-Gd** and **5-Er** support the field-induced SMM behaviour observed from the experiment.

A correlation has been developed to compare the energy barriers from single-ion relaxation of lanthanide ions, the exchange-coupled states mechanism, and experimental data with the Ru^{III}–Ln^{III} J values (Fig. 8). At the single-ion level, the first excited KDs/IDs values are taken considering a low QTM and tunneling gap that allows relaxation in those states, or it could be quenched upon exchange or application of a dc field. The correlation suggests that **3-Dy** has a better U_{cal}/U_{eff} than other complexes, which could be attributed to the combination of oblate electron density that favors axial anisotropy and a moderate J (Ru–Ln) value. This balance between electron

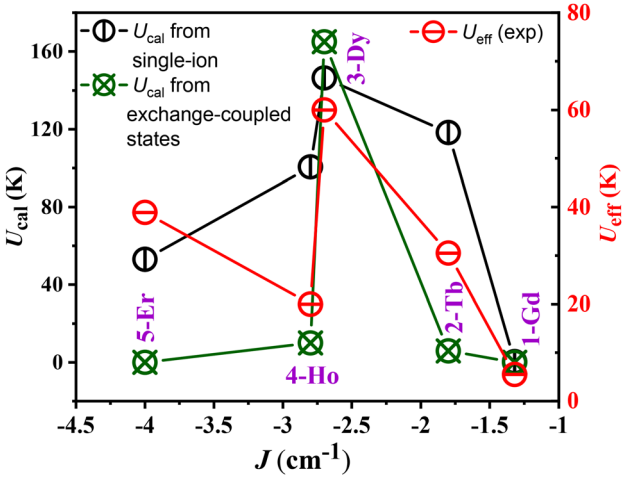

Fig. 8 Comparison of exchange interaction (J, cm^{-1}) with experimental energy barrier (U_{eff}, K) and computed energy barrier from single-ion as well as exchange-coupled states (U_{cal}, K) of **1-Gd**, **2-Tb**, **3-Dy**, **4-Ho**, and **5-Er**.

density distribution and exchange strength stabilizes the relaxation barrier and enhances SMM behaviour. For the **2-Tb** and **4-Ho**, the U_{eff} falls between the U_{cal} from single-ion and U_{cal} from coupled-states, which hints that the tunneling gap between the ground IDs of oblate Tb^{III} and Ho^{III} ions is quenched with the combined effect of moderate $J_{1(Ru–Ln)}$ value and an applied dc magnetic field. Though **5-Er** has a greater J value among all, the prolate electron density disfavors the exchange-coupled relaxation and leads to weak SMM behaviour even upon the application of a dc field. Hence, in the Er analogue, the exchange interactions are insufficient to effectively separate the excited states, which therefore remain closer in energy to the single-ion levels, further limiting its performance. Overall, due to strong Ru···Ln exchange interactions, the U_{cal} value derived from the POLY_ANISO computations of all the complexes was improved compared to their single-ion computations. For example: (i) for **3-Dy** the U_{cal} of the individual Dy^{III} ion is 101.8 cm^{-1}, which has increased to 111 cm^{-1} when they are coupled with the Ru^{III} ion; (ii) for **2-Tb** and **4-Ho** at the single-ion level, both the Tb^{III} and Ho^{III} ions, showed a large tunneling gap in their GS itself, which was quenched when they coupled with Ru^{III} ions and yielded reasonable energy barrier of 3.9 cm^{-1} and 6.9 cm^{-1}, respectively, importantly we observed zero-field SMM behaviour for **4-Ho**, highlighting the importance of the exchange interaction; (iii) the larger QTM observed between the ground KDs of Er^{III} ion was also quenched to some extent in the exchange-coupled mechanism; (iv) for **1-Gd** the isotropic Gd^{III} ions coupled with the anisotropic Ru^{III} ions with a moderate Ru–Gd exchange interaction resulted in a ground state value of S = 6, and showed SMM behavior, becoming a rare example of Gd-based SMMs.[70,71]

The observed higher centrosymmetric space group $P\bar{1}$, in these complexes, seemingly, brought small geometric changes with different lanthanide ions that have significant effects on

the balance between anisotropy and magnetic exchange interactions, even though the overall crystallographic symmetry is invariant. Such an effect of symmetry and space groups of crystal structures usually has an important influence on magnetism, which was proven by single-crystal measurements for a few 3d–4f complexes;[62] however, our detailed *ab initio* calculations provide an adequate explanation here. For example, a stronger transverse anisotropy component is introduced by the **5-Er**, which significantly increases the QTM. Conversely, the **3-Dy** and **4-Ho** that contain Dy and Ho exhibit a more axial form of anisotropy, favoring slower, thermally induced relaxation pathways. Additionally, determining the magnetic exchange between the metal centres is largely dependent on the spatial arrangement and relative orientation of the Ln···Ln vectors as well as the Ru–Ln exchange pathways integrated into the inversion-symmetric $P\bar{1}$ space group. The intricate interactions among global symmetry, exchange topology, and local coordination geometry in controlling the single-ion and collective magnetic characteristics of this Ru–Ln compound family are emphasised in this study.

As stated earlier, some of us reported $\{Ru^{III}_2Dy^{III}_2\}$ butterfly complexes bearing energy barriers of 15.4 K (ref. 45) and 45 K.[47] In the present work, the effective energy barrier is enhanced to 60 K in **3-Dy** due to the improvement of the magnetic exchange interaction between $Ru^{III}\cdots Dy^{III}$ from -2.4 cm^{-1} to -2.7 cm^{-1}, which can be attributed to the presence of more acidic *o*-toluate ligands, which helped to provide better alignment of anisotropic directions compared with the previously reported benzoate $\{Ru^{III}_2Dy^{III}_2\}$ analog.[45,47] In the previously reported cases, the anisotropic directions of Dy···Dy ions are aligned parallel with the Ru···Ru anisotropic direction. However, in **3-Dy**, these anisotropic directions are not completely parallel to each other, which eventually helps in the enhancement of the 4d–4f exchange interaction.

Compared to 3d–4f magnetic exchange interaction as explored in $\{Cr^{III}_2Dy^{III}_2\}$ complexes, the $Ru^{III}\cdots Ln^{III}$ exchange interaction is found to be smaller, irrespective of the ligand and Ln^{III} metal ions used. For example, the $[Cr^{III}_2Dy^{III}_2(OMe)_2(O_2CPh)_4(mdea)_2(NO_3)_2]$ complex[27] shows Cr^{III}–Dy^{III} magnetic exchange interaction (J) of -20.7 to -16.3 cm^{-1} with U_{eff} = 54 cm^{-1} and T_B = 3.7 K, and $[Cr^{III}_2Dy^{III}_2(OMe)_2(acac)_4(mdea)_2(NO_3)_2]$, shows J (Cr–Dy) of -11.2 to -8.3 cm^{-1} with U_{eff} = 24 cm^{-1} and T_B = 1.8 K.[28] The J values are better compared to the reported Ru–Ln complexes; however, the U_{eff} values are similar to the Ru^{III}–Dy^{III} complexes. This is because the Ru^{III} ion not only participates in the exchange interaction but also lifts the degeneracy of the crystal-field splitting due to its anisotropic nature, improving the magnetization reversal barrier. Whereas the Cr^{III} ion is isotropic, which helps only in the exchange part.

Conclusions

We demonstrated the utilization of the magnetic exchange interactions and magnetic anisotropies in quenching QTM in five $\{Ru^{III}_2Ln^{III}_2\}$ butterfly complexes (**1-Gd**, **2-Tb**, **3-Dy**, **4-Ho**, and **5-Er**) by detailed experimental and computational studies. Among them, **2-Tb**, **4-Ho**, and **5-Er** are the first set of non-Dy^{III}-based Ru-4f complexes. AC magnetic studies suggested that **3-Dy** and **4-Ho** show slow magnetic relaxation in the absence of an external magnetic field with U_{eff} of 60 K and 20 K, respectively. Whereas **1-Gd**, **2-Tb**, and **5-Er** show field-induced SMM behavior with a U_{eff} of 5.5 K, 30.5 K, and 38.9 K, under an applied dc field of 3600 Oe, 2000 Oe, and 2400 Oe, respectively. An anisotropy barrier (U_{eff}) of 60 K was determined for **3-Dy**, representing the highest value reported to date for 4d–4f butterfly-type complexes. For **4-Ho**, zero-field SMM behavior is recognized, which is a rare occurrence for complexes containing this ion due to the usual large QTM, making it a unique addition of a zero-field Ho^{III} SMM and the first {Ru–Ln} SMM not containing a Dy^{III} ion. Additionally, the field-induced SMM for **1-Gd** is a rare Gd-based SMM and expands the diversity of heterometallic complexes in the field of molecular magnetism. The CASSCF/SO-RASSI/SINGLE_ANISO/POLY_ANISO/DFT calculations support the experimental observation of SMM behavior for all five complexes. These calculations predict that the Ru···Ln exchange interaction plays a major role in enhancing the barrier height and quenching QTM in the case of **1-Gd**, **2-Tb**, **3-Dy**, and **4-Ho**, demonstrating the potential of using Ru^{III} ions in SMM design.

Overall, the present work reveals that a strong magnetic exchange interaction can be found between Ru^{III} and Ln^{III} ions (-0.4 to -4 cm^{-1}), and highlights the importance of the $Ru^{III}\cdots Ln^{III}$ magnetic exchange interaction for observing SMM behaviour with Ln^{III} ions such as Dy^{III} and Ho^{III}. The dominant Ru–Ln exchange interaction progresses from **5-Er** to **4-Ho**, **3-Dy**, **2-Tb**, and **1-Gd**, and this pattern is correlated to the number of orbital overlaps that determines the magnitude of the Ru-Ln exchange interaction. Furthermore, we showed improvements of the effective anisotropy barrier compared to previously reported $\{Ru^{III}_2Dy^{III}_2\}$ butterfly complexes by increasing the exchange interaction *via* ligand manipulation.[45,47]

Experimental and computational methodologies

Synthesis procedures

Materials and methods. All reactions were conducted under aerobic conditions. Reagents and solvents were sourced commercially and utilized without additional purification.

Synthesis of $[Ru^{III}_2Gd^{III}_2(OMe)_2(o\text{-tol})_4(mdea)_2(NO_3)_2]$ (1-Gd). A similar method to that used to make $[Ru^{III}_2Dy^{III}_2(OMe)_2(O_2CPh)_4(mdea)_2(NO_3)_2]$ was employed.[45,47] $RuCl_3{\cdot}xH_2O$ (0.25 mmol) and $Gd(NO_3)_3{\cdot}6H_2O$ (0.25 mmol) were dissolved in 15 mL of acetonitrile (MeCN). *ortho*-Toluic acid (0.5 mmol), *N*-methyldiethanolamine (0.25 mmol), and triethylamine (1.0 mmol) were then added, resulting in a dark brown solution while being heated to 60 °C. The mixture was stirred at this temperature for 6 hours, after which the solvent was evaporated, leaving behind a brown oil. This brown oil was re-dis-

solved in methanol (MeOH) and layered with diethyl ether (Et_2O). Within 2 weeks, brown crystals were isolated, which are suitable for single-crystal X-ray diffraction. Brown-coloured crystals of **1-Gd** appeared within 2 weeks, with an approximate yield (based on $Gd(NO_3)_3$ of **1-Gd**) of 47% (crystalline product). Anal. Calculated (found) for **1-Gd**: $Ru_2Gd_2C_{44}H_{56}O_{20}N_4$: C, 35.77 (35.55); H, 3.82 (3.54); N, 3.79 (3.51). IR (KBr, cm^{-1}): 3432 (m), 3063 (w), 2959 (w), 2928 (w), 2863 (w), 2826 (w), 1606 (m), 1583 (m), 1553 (s), 1463 (s), 1441 (w), 1383 (s), 1300 (m), 1157 (w), 1061 (m), 1010 (m), 900 (w), 857 (w), 814 (w), 788 (w), 741 (m), 669 (w), 612 (w).

Synthesis of $[Ru^{III}_2Tb^{III}_2(OMe)_2(o\text{-tol})_4(mdea)_2(NO_3)_2]$ (2-Tb). The synthetic method for **1-Gd** was carried out, but $Tb(NO_3)_3{\cdot}6H_2O$ (0.25 mmol) was used instead of $Gd(NO_3)_3{\cdot}6H_2O$. Brown-coloured crystals of **2-Tb** appeared within 2 weeks, with an approximate yield (based on $Tb(NO_3)_3$ of **2-Tb**) of 45% (crystalline product). Anal. Calculated (found) for **2-Tb**: $Ru_2Tb_2C_{44}H_{56}O_{20}N_4$: C, 35.69 (35.60); H, 3.81 (3.76); N, 3.78 (3.89). IR (KBr, cm^{-1}): 3432 (m), 3063 (w), 2959 (w), 2926 (w), 2863 (w), 2824 (w), 1606 (m), 1583 (m), 1555 (s), 1461 (s), 1439 (w), 1381 (s), 1302 (m), 1155 (w), 1061 (m), 1010 (m), 900 (w), 857 (w), 788 (w), 741 (m), 669 (w), 610 (w), 514 (w).

Synthesis of $[Ru^{III}_2Dy^{III}_2(OMe)_2(o\text{-tol})_4(mdea)_2(NO_3)_2]$ (3-Dy). The synthetic method for **1-Gd** was carried out, but $Dy(NO_3)_3{\cdot}6H_2O$ (0.25 mmol) was used instead of $Gd(NO_3)_3{\cdot}6H_2O$. Within 2 weeks, brown crystals were isolated, which are suitable for single-crystal X-ray diffraction. Yield (based on $Dy(NO_3)_3$) of **3-Dy** = 42% (crystalline product). Elemental Analysis: calculated (found) for **3-Dy**: $Ru_2Dy_2C_{44}H_{56}O_{20}N_4$: C, 35.51 (35.60); H, 3.79 (3.51); N, 3.77 (4.01). IR (KBr, cm^{-1}): 3430 (m), 3061 (w), 2963 (w), 2930 (w), 2863 (w), 2828 (w), 1606 (m), 1583 (m), 1553 (s), 1465 (s), 1441 (w), 1381 (s), 1302 (m), 1157 (w), 1061 (m), 1010 (m), 902 (w), 855 (w), 816 (w), 790 (w), 741 (m), 669 (w), 610 (w).

Synthesis of $[Ru^{III}_2Ho^{III}_2(OMe)_2(o\text{-tol})_4(mdea)_2(NO_3)_2]$ (4-Ho). The synthetic method for **1-Gd** was carried out, but $Ho(NO_3)_3{\cdot}5H_2O$ (0.25 mmol) was used instead of $Gd(NO_3)_3{\cdot}6H_2O$. Brown-coloured crystals of **4-Ho** appeared within 2 weeks, with an approximate yield (based on $Ho(NO_3)_3$ of **4-Ho**) of 47% (crystalline product). Anal. Calculated (found) for **4-Ho**: $Ru_2Ho_2C_{44}H_{56}O_{20}N_4$: C, 35.40 (35.73); H, 3.78 (3.31); N, 3.75 (4.21). IR (KBr, cm^{-1}): 3432 (m), 3063 (w), 2961 (w), 2930 (w), 2863 (w), 2828 (w), 1606 (m), 1583 (m), 1553 (s), 1467 (s), 1441 (w), 1381 (s), 1304 (m), 1157 (w), 1059 (m), 1010 (m), 902 (w), 857 (w), 816 (w), 790 (w), 741 (m), 669 (w), 610 (w).

Synthesis of $[Ru^{III}_2Er^{III}_2(OMe)_2(o\text{-tol})_6(mdea)_2]{\cdot}2MeOH$ (5-Er). The synthetic method for **1-Gd** was carried out, but $Er(NO_3)_3{\cdot}5H_2O$ (0.25 mmol) was used instead of $Gd(NO_3)_3{\cdot}6H_2O$. Brown-coloured crystals of **5-Er** appeared within 2 weeks, with an approximate yield (based on $Er(NO_3)_3$ of **5-Er**) of 45% (crystalline product). Anal. Calculated (found) for **5-Er**: $Ru_2Er_2C_{61}H_{74}O_{19}N_2$: C, 43.60 (43.23); H, 4.60 (4.53); N, 1.64 (1.91). IR (KBr, cm^{-1}): 3432 (m), 3063 (w), 2957 (w), 2930 (w), 2863 (w), 2828 (w), 1606 (m), 1583 (m), 1553 (s), 1467 (s), 1439 (w), 1381 (s), 1306 (m), 1157 (w), 1061 (m), 1008 (m), 902 (w), 857 (w), 816 (w), 786 (w), 743 (m), 669 (w), 614 (w), 514 (w).

X-ray crystallography

Single-crystal X-ray diffraction data for **3-Dy**, **4-Ho**, and **5-Er** were collected using a Bruker diffractometer with Mo Kα radiation (λ = 0.71073 Å). Crystals were selected under mineral oil, mounted on fiber loops, and cooled using an Oxford Cryo-system. A complete hemispherical dataset was acquired using ω and φ scan techniques (1° per frame, 2 seconds per frame). Cell refinement and data reduction were carried out using CrysAlisPro 1.171.38.43. The structures were solved by direct methods and refined by full-matrix least-squares techniques on F^2 using SHELXL as implemented in Olex2-1.5. All non-hydrogen atoms were refined anisotropically, while hydrogen atoms were placed in calculated positions and refined using a riding model. The CCDC numbers are 2456392–2456394. Crystallographic data and refinement parameters are summarized in Table S1 in the SI.

Powder X-ray diffraction (PXRD) data for **1-Gd** and **2-Tb**, as well as for other samples, were collected on a Rigaku Ultima IV fully automatic high-resolution X-ray diffractometer system with a Theta–Theta (θ–θ) Goniometer, which was utilized for routine characterization of powder samples. Scans were performed at room temperature in the 2θ range 5–50° and compared with predicted patterns based on low-temperature single-crystal X-ray data.

Magnetic measurements

Magnetic susceptibility measurements were carried out on a Quantum Design SQUID magnetometer MPMS-3 and PPMS, operated between 1.8 and 300 K for DC-applied fields ranging from 0 to 70 kOe and 0 to 90 kOe, respectively. To prevent the crystallites from torquing, microcrystalline samples were distributed in Vaseline. A calibrated gelatin capsule containing the sample mulls was fixed at the end of the sample rod and held in the middle of a drinking straw. Alternating current (AC) magnetic susceptibility measurements were carried out under an oscillating AC field with frequencies ranging from 0.1 Hz to 1 kHz (MPMS-3) and 10 Hz to 10 kHz (PPMS).

Computational details

***Ab initio* calculations.** The *ab initio* calculations were performed using MOLCAS 8.2[72] on the anisotropic metal ions Tb^{III}, Dy^{III}, Ho^{III}, Er^{III}, and Ru^{III} in complexes **2-Tb**, **3-Dy**, **4-Ho**, and **5-Er**. Calculations for **3-Dy**, **4-Ho**, and **5-Er** were performed using their X-ray structures, whereas for **2-Tb**, the X-ray structure of **3-Dy** was utilized by replacing Dy^{III} with Tb^{III}. The Douglas-Kroll Hamiltonian is employed to incorporate relativistic effects.[73] The Complete Active Space Self-Consistent Field (CASSCF) method is employed to compute the spin-free eigenstates.[74] The following basis sets are used for the respective metal ions such as [ANO-RCC...8s7p5d3f2g1h.] basis set for paramagnetic Ln(III) ions, [ANO-RCC...7s6p4d3f1g.] for Lu(III), [ANO-RCC...6s5p3d1f.] for Ru(III) ion, [ANO-RCC...6s5p3d.] for Y(III) ion, [ANO-RCC...3s2p.] for C atoms, [ANO-RCC...3s2p.] for N atoms, [ANO-RCC...4s3p2d.] for O atoms and [ANO-RCC...2s.] for H atoms.[75] The neighboring Ln^{III} (Tb^{III}, Dy^{III}, Ho^{III}, and Er^{III}) and Ru^{III} ions were replaced by diamagnetic Lu^{III}

and Y^{III}, respectively, while performing the single-ion calculations. In the CASSCF calculations, the active spaces (8,7), (9,7), (10,7), and (11,7) were considered for the Tb^{III}, Dy^{III}, Ho^{III}, and Er^{III} ions, respectively, and (5,5) in the case of Ru^{III} ion. To compute the SOC, 7 septet, 140 quintet, and 195 triplet states for Tb^{III}; 21 sextet, 224 quartet, and 490 doublet states for Dy^{III}; 35 quintet, 210 triplet, and 195 singlet states for Ho^{III}; and 35 quartet and 112 doublet states for Er^{III}; and 1 sextet, 24 quartet, and 75 doublet states for Ru^{III} were considered. After calculating the excited spin–orbit states, we mixed the roots that are below 50000 cm^{-1} using RASSI-SO.[51] Moreover, the mixed spin–orbit (SO) states were used in the SINGLE_ANISO program to calculate the *g*-tensors.[76] We have also determined the crystal-field parameters using the SINGLE_ANISO module in MOLCAS 8.2 by following the equation below.

$$\widehat{H}_{CF} = \sum \sum_{k=-q}^{q} B_q^k \tilde{O}_k^q \quad (3)$$

POLY_ANISO calculations. The observed magnetic data for each complex were analyzed using the POLY_ANISO software[48–50] within the Lines model to determine the exchange interaction between the metal ions (eqn (4)).

$$\widehat{H}_{ex} = -\sum_{i=1}^{3} J_i S_i S_{i+1} \quad (4)$$

(here $J_i = J_i^{dipolar} + J_i^{exch}$; *i.e.*, J_i is the total magnetic interaction of the fitted $J_i^{dipolar}$ and J_i^{exch} parameters).

Density functional theory (DFT) calculations. To compute the exchange interactions in the Gd analog (**1-Gd**), DFT calculations were performed using the B3LYP functional[77] within the Gaussian 16 software package.[61] BS-DFT calculations were performed by utilizing the X-ray structure of **3-Dy** and replacing Dy^{III} with Gd^{III}, while the positions of the other atoms were kept consistent with those determined by X-ray crystallography. We employed the Cundari–Stevens (CS) relativistic effective core potential (ECP) on Gd,[78] def2-TZVP basis set for Ru, 6-31G** basis set for C, N, O, H. The magnetic exchange (J) values were calculated using the Broken Symmetry (BS) method[60] in association with DFT computations.

The exchange interaction (J) is calculated by using the following Hamiltonian:

$$\widehat{H} = \left[2J_1\left(\vec{S}_{Gd1}\vec{S}_{Ru1} + \vec{S}_{Gd2}\vec{S}_{Ru1} + \vec{S}_{Gd1}\vec{S}_{Ru2} + \vec{S}_{Gd2}\vec{S}_{Ru2}\right) + 2J_2\left(\vec{S}_{Gd1}\vec{S}_{Gd2}\right) + 2J_3\left(\vec{S}_{Ru1}\vec{S}_{Ru2}\right)\right] \quad (5)$$

Conflicts of interest

There are no conflicts to declare.

Data availability

All data supporting the findings of this study are included in the supplementary information (SI). Supplementary information: crystallographic data, PXRD, magnetic plots and tables, and computational analysis plots and tables. See DOI: https://doi.org/10.1039/d5qi01665g.

CCDC 2456392–2456394 contain the supplementary crystallographic data for this paper.[79a–c]

Acknowledgements

I. J. D. thanks the DST-INSPIRE (IF220060) for providing a PhD fellowship. V. K. is thankful to the Prime Minister's Research Fellowship for financial assistance. M. S. thanks the funding agencies SERB (CRG/2023/002178), BRNS (58/14/07/2023-BRNS/37029), CSIR (01/3092/23/EMR-II), IISc-STARs (MoE-STARS/STARS-2/2023-0158), and IIT Bombay for the financial support. K. R. V. thanks the IISER Mohali-Central PXRD facility, IISER Mohali-High-Performance Computing Facility, and Prof. Gopalan Rajaraman, IIT Bombay, for providing computing resources. K. R. V. also thanks SERB for providing start-up research grant funding (SRG/2023/000286).

References

1 M. N. Leuenberger and D. Loss, Quantum computing in molecular magnets, *Nature*, 2001, **410**, 789–793.
2 A. Ardavan, O. Rival, J. J. L. Morton, S. J. Blundell, A. M. Tyryshkin, G. A. Timco and R. E. P. Winpenny, Will spin-relaxation times in molecular magnets permit quantum information processing?, *Phys. Rev. Lett.*, 2007, **98**, 057201.
3 S. Thiele, F. Balestro, R. Ballou, S. Klyatskaya, M. Ruben and W. Wernsdorfer, Electrically driven nuclear spin resonance in single-molecule magnets, *Science*, 2014, **344**, 1135–1138.
4 J. M. Zadrozny, J. Niklas, O. G. Poluektov and D. E. Freedman, Millisecond coherence time in a tunable molecular electronic spin qubit, *ACS Cent. Sci.*, 2015, **1**, 488–492.
5 M. Shiddiq, D. Komijani, Y. Duan, A. Gaita-Ariño, E. Coronado and S. Hill, Enhancing coherence in molecular spin qubits via atomic clock transitions, *Nature*, 2016, **531**, 348–351.
6 M. F. Crommie, Manipulating magnetism in a single molecule, *Science*, 2005, **309**, 1501–1502.
7 M. Urdampilleta, N.-V. Nguyen, J.-P. Cleuziou, S. Klyatskaya, M. Ruben and W. Wernsdorfer, Molecular quantum spintronics: Supramolecular spin valves based on single-molecule magnets and carbon nanotubes, *Int. J. Mol. Sci.*, 2011, **12**, 6656–6667.
8 L. E. Darago, M. D. Boshart, B. D. Nguyen, E. Perlt, J. W. Ziller, W. W. Lukens, F. Furche, W. J. Evans and J. R. Long, Strong ferromagnetic exchange coupling and single-molecule magnetism in MoS_4^{3-}-bridged dilanthanide complexes, *J. Am. Chem. Soc.*, 2021, **143**, 8465–8475.
9 A. Swain, T. Sharma and G. Rajaraman, Strategies to quench quantum tunneling of magnetization in lanthanide

single molecule magnets, *Chem. Commun.*, 2023, **59**, 3206–3228.
10 R. Sessoli, D. Gatteschi, A. Caneschi and M. A. Novak, Magnetic bistability in a metal-ion cluster, *Nature*, 1993, **365**, 141–143.
11 R. Tiron, W. Wernsdorfer, N. Aliaga-Alcalde and G. Christou, Quantum tunneling in a three-dimensional network of exchange-coupled single-molecule magnets, *Phys. Rev. B: Condens. Matter Mater. Phys.*, 2003, **68**, 140407.
12 J. D. Rinehart, M. Fang, W. J. Evans and J. R. Long, Strong exchange and magnetic blocking in N_2^{3-}-radical-bridged lanthanide complexes, *Nat. Chem.*, 2011, **3**, 538–542.
13 Y. Peng and A. K. Powell, What do 3d–4f butterflies tell us?, *Coord. Chem. Rev.*, 2021, **426**, 213490.
14 N. Ishikawa, M. Sugita, T. Ishikawa, S.-y. Koshihara and Y. Kaizu, Mononuclear lanthanide complexes with a long magnetization relaxation time at high temperatures: A new category of magnets at the single-molecular level, *J. Phys. Chem. B*, 2004, **108**, 11265–11271.
15 F.-S. Guo, B. M. Day, Y.-C. Chen, M.-L. Tong, A. Mansikkamäki and R. A. Layfield, Magnetic hysteresis up to 80 kelvin in a dysprosium metallocene single-molecule magnet, *Science*, 2018, **362**, 1400–1403.
16 A. H. Vincent, Y. L. Whyatt, N. F. Chilton and J. R. Long, Strong axiality in a dysprosium(III) bis (borolide) complex leads to magnetic blocking at 65 K, *J. Am. Chem. Soc.*, 2023, **145**, 1572–1579.
17 S. K. Gupta, T. Rajeshkumar, G. Rajaraman and R. Murugavel, An air-stable Dy(III) single-ion magnet with high anisotropy barrier and blocking temperature, *Chem. Sci.*, 2016, **7**, 5181–5191.
18 A. B. Canaj, S. Dey, E. R. Martí, C. Wilson, G. Rajaraman and M. Murrie, Insight into D_{6h} Symmetry: Targeting Strong Axiality in Stable Dysprosium(III) Hexagonal Bipyramidal Single–Ion Magnets, *Angew. Chem., Int. Ed.*, 2019, **58**, 14146–14151.
19 A. S. Armenis, A. Mondal, S. R. Giblin, C. P. Raptopoulou, V. Psycharis, D. I. Alexandropoulos, J. Tang, R. A. Layfield and T. C. Stamatatos, Unveiling new [1 + 1] Schiff-base macrocycles towards high energy-barrier hexagonal bipyramidal Dy(III) single-molecule magnets, *Chem. Commun.*, 2024, **60**, 12730–12733.
20 A. S. Armenis, A. Mondal, S. R. Giblin, D. I. Alexandropoulos, J. Tang, R. A. Layfield and T. C. Stamatatos, 'Kick-in the head': high-performance and air-stable mononuclear Dy^{III} single-molecule magnets with pseudo-D_{6h} symmetry from a [1 + 1] Schiff-base macrocycle approach, *Inorg. Chem. Front.*, 2025, **12**, 1214–1224.
21 H. Kwon, K. R. McClain, J. G. C. Kragskow, J. K. Staab, M. Ozerov, K. R. Meihaus, B. G. Harvey, E. S. Choi, N. F. Chilton and J. R. Long, Coercive fields exceeding 30 T in the mixed-valence single-molecule magnet $(Cp^{iPr5})_2Ho_2I_3$, *J. Am. Chem. Soc.*, 2024, **146**, 18714–18721.
22 C. A. Gould, K. R. McClain, D. Reta, J. G. C. Kragskow, D. A. Marchiori, E. Lachman, E.-S. Choi, J. G. Analytis, R. D. Britt and N. F. Chilton, Ultrahard magnetism from mixed-valence dilanthanide complexes with metal-metal bonding, *Science*, 2022, **375**, 198–202.
23 D. N. Woodruff, R. E. P. Winpenny and R. A. Layfield, Lanthanide single-molecule magnets, *Chem. Rev.*, 2013, **113**, 5110–5148.
24 L. R. Piquer and E. C. Sañudo, Heterometallic 3d–4f single-molecule magnets, *Dalton Trans.*, 2015, **44**, 8771–8780.
25 K. Liu, W. Shi and P. Cheng, Toward heterometallic single-molecule magnets: Synthetic strategy, structures and properties of 3d–4f discrete complexes, *Coord. Chem. Rev.*, 2015, **289**, 74–122.
26 J. L. Liu, J. Y. Wu, Y. C. Chen, V. Mereacre, A. K. Powell, L. Ungur, L. F. Chibotaru, X. M. Chen and M. L. Tong, A heterometallic Fe^{II}–Dy^{III} single–molecule magnet with a record anisotropy barrier, *Angew. Chem., Int. Ed.*, 2014, **53**, 12966–12970.
27 S. K. Langley, D. P. Wielechowski, V. Vieru, N. F. Chilton, B. Moubaraki, B. F. Abrahams, L. F. Chibotaru and K. S. Murray, A $\{Cr^{III}_2Dy^{III}_2\}$ single-molecule magnet: enhancing the blocking temperature through 3d magnetic exchange, *Angew. Chem., Int. Ed.*, 2013, **52**, 12014–12019.
28 S. K. Langley, D. P. Wielechowski, V. Vieru, N. F. Chilton, B. Moubaraki, L. F. Chibotaru and K. S. Murray, Modulation of slow magnetic relaxation by tuning magnetic exchange in $\{Cr_2Dy_2\}$ single molecule magnets, *Chem. Sci.*, 2014, **5**, 3246–3256.
29 S. K. Langley, D. P. Wielechowski, B. Moubaraki and K. S. Murray, Enhancing the magnetic blocking temperature and magnetic coercivity of $\{Cr^{III}_2Ln^{III}_2\}$ single-molecule magnets via bridging ligand modification, *Chem. Commun.*, 2016, **52**, 10976–10979.
30 S. K. Langley, C. M. Forsyth, B. Moubaraki and K. S. Murray, A fluoride bridged $\{Cr^{III}_4Dy^{III}_4\}$ single molecule magnet, *Dalton Trans.*, 2015, **44**, 912–915.
31 S. K. Langley, N. F. Chilton, B. Moubaraki and K. S. Murray, Single-molecule magnetism in three related $\{Co^{III}_2Dy^{III}_2\}$-acetylacetonate complexes with multiple relaxation mechanisms, *Inorg. Chem.*, 2013, **52**, 7183–7192.
32 K. R. Vignesh, S. K. Langley, K. S. Murray and G. Rajaraman, Quenching the Quantum Tunneling of Magnetization in Heterometallic Octanuclear $\{TM^{III}_4Dy^{III}_4\}$ (TM = Co and Cr) Single–Molecule Magnets by Modification of the Bridging Ligands and Enhancing the Magnetic Exchange Coupling, *Chem. – Eur. J.*, 2017, **23**, 1654–1666.
33 D. Schray, G. Abbas, Y. Lan, V. Mereacre, A. Sundt, J. Dreiser, O. Waldmann, G. E. Kostakis, C. E. Anson and A. K. Powell, Combined magnetic susceptibility measurements and ^{57}Fe mössbauer spectroscopy on a ferromagnetic $\{Fe^{III}_4Dy_4\}$ ring, *Angew. Chem., Int. Ed.*, 2010, **49**, 5185–5188.
34 Y. Peng, J. Braun, M. Schulze, H. Kaemmerer, Y. F. Schneider, C. E. Anson, W. Wernsdorfer and A. K. Powell, A nested spin structure and single molecule magnet behaviour in an Fe_8Dy_{12} heterometallic cyclic coordination cluster, *Dalton Trans.*, 2024, **53**, 894–897.

35 N. Ahmed, C. Das, S. Vaidya, S. K. Langley, K. S. Murray and M. Shanmugam, Nickel(II)–Lanthanide (III) Magnetic Exchange Coupling Influencing Single–Molecule Magnetic Features in $\{Ni_2Ln_2\}$ Complexes, *Chem. – Eur. J.*, 2014, **20**, 14235–14239.

36 V. Chandrasekhar, P. Bag, W. Kroener, K. Gieb and P. Müller, Pentanuclear heterometallic $\{Ni_2Ln_3\}$(Ln = Gd, Dy, Tb, Ho) assemblies. Single-molecule magnet behavior and multistep relaxation in the dysprosium derivative, *Inorg. Chem.*, 2013, **52**, 13078–13086.

37 M. Li, Y. Lan, A. M. Ako, W. Wernsdorfer, C. E. Anson, G. Buth, A. K. Powell, Z. Wang and S. Gao, A family of 3d–4f octa-nuclear $[Mn^{III}_4Ln^{III}_4]$ wheels (Ln = Sm, Gd, Tb, Dy, Ho, Er, and Y): synthesis, structure, and magnetism, *Inorg. Chem.*, 2010, **49**, 11587–11594.

38 K. R. Vignesh, S. K. Langley, B. Moubaraki, K. S. Murray and G. Rajaraman, Large hexadecametallic $\{Mn^{III}–Ln^{III}\}$ wheels: Synthesis, structural, magnetic, and theoretical characterization, *Chem. – Eur. J.*, 2015, **21**, 16364–16369.

39 C. Benelli and D. Gatteschi, *Introduction to molecular magnetism: From transition metals to lanthanides*, John Wiley & Sons, 2015.

40 C. Kremer, Substitution on Re(IV) complexes: a tool for the synthesis of novel mono-and polynuclear compounds, *Commun. Inorg. Synth.*, 2013, **1**, 8–15.

41 T. D. Harris, M. V. Bennett, R. Clerac and J. R. Long, $[ReCl_4(CN)_2]^{2-}$: A high magnetic anisotropy building unit giving rise to the single-chain magnets $(DMF)_4MReCl_4(CN)_2$ (M = Mn, Fe, Co, Ni), *J. Am. Chem. Soc.*, 2010, **132**, 3980–3988.

42 X.-Y. Wang, C. Avendaño and K. R. Dunbar, Molecular magnetic materials based on 4d and 5d transition metals, *Chem. Soc. Rev.*, 2011, **40**, 3213–3238.

43 S. K. Singh and G. Rajaraman, Deciphering the origin of giant magnetic anisotropy and fast quantum tunnelling in Rhenium(IV) single-molecule magnets, *Nat. Commun.*, 2016, **7**, 10669.

44 A. Upadhyay, J. Rajpurohit, M. Kumar Singh, R. Dubey, A. Kumar Srivastava, A. Kumar, G. Rajaraman and M. Shanmugam, Hydroxo–Bridged Dimers of Oxo–Centered Ruthenium(III) Triangle: Synthesis and Spectroscopic and Theoretical Investigations, *Chem. – Eur. J.*, 2014, **20**, 6061–6070.

45 S. K. Langley, D. P. Wielechowski, V. Vieru, N. F. Chilton, B. Moubaraki, L. F. Chibotaru and K. S. Murray, The first 4d/4f single-molecule magnet containing a $\{Ru^{III}_2Dy^{III}_2\}$ core, *Chem. Commun.*, 2015, **51**, 2044–2047.

46 M. R. Saber and K. R. Dunbar, Trigonal bipyramidal 5d–4f molecules with SMM behavior, *Chem. Commun.*, 2014, **50**, 2177–2179.

47 A. Swain, R. Martin, K. R. Vignesh, G. Rajaraman, K. S. Murray and S. K. Langley, Enhancing the barrier height for magnetization reversal in 4d/4f $Ru^{III}_2Ln^{III}_2$ "butterfly" single molecule magnets (Ln = Gd, Dy) via targeted structural alterations, *Dalton Trans.*, 2021, **50**, 12265–12274.

48 L. Chibotaru, L. Ungur and A. Soncini, The origin of non-magnetic Kramers doublets in the ground state of dysprosium triangles: evidence for a toroidal magnetic moment, *Angew. Chem., Int. Ed.*, 2008, **47**, 4126–4129.

49 L. Ungur, W. Van den Heuvel and L. F. Chibotaru, *Ab initio* investigation of the non-collinear magnetic structure and the lowest magnetic excitations in dysprosium triangles, *New J. Chem.*, 2009, **33**, 1224–1230.

50 L. F. Chibotaru, L. Ungur, C. Aronica, H. Elmoll, G. Pilet and D. Luneau, Structure, magnetism, and theoretical study of a mixed-valence $Co^{II}_3Co^{III}_4$ heptanuclear wheel: lack of SMM behavior despite negative magnetic anisotropy, *J. Am. Chem. Soc.*, 2008, **130**, 12445–12455.

51 N. F. Chilton, R. P. Anderson, L. D. Turner, A. Soncini and K. S. Murray, PHI: A powerful new program for the analysis of anisotropic monomeric and exchange–coupled polynuclear d-and f-block complexes, *J. Comput. Chem.*, 2013, **34**, 1164–1175.

52 D. Reta and N. F. Chilton, Uncertainty estimates for magnetic relaxation times and magnetic relaxation parameters, *Phys. Chem. Chem. Phys.*, 2019, **21**, 23567–23575.

53 B. Dutta, T. Guizouarn, A. Gharu, F. Pointillart, K. R. Vignesh and D. Ray, New Family of Dinuclear Ni–Ln Complexes from Ternary Coordination by β-Diketonates around the Lanthanoids: Synthesis, Structures, and Magnetic Behavior with Theoretical Supports, *Cryst. Growth Des.*, 2024, **25**, 143–157.

54 N. Barman, P. Halder, S. Mukhopadhyay, B. Schwarz, E. Colacio, R. Rana, G. Rajaraman and J. Goura, Synthesis, structure, and magnetic properties of diamagnetic Co (iii) ion-based heterometallic $Co^{III}–Ln^{III}$ (Ln = Dy, Tb, Ho, Er) complexes, *New J. Chem.*, 2024, **48**, 15735–15746.

55 S. K. Gupta, T. Rajeshkumar, G. Rajaraman and R. Murugavel, Is a strong axial crystal-field the only essential condition for a large magnetic anisotropy barrier? The case of non-Kramers Ho(III) versus Tb(III), *Dalton Trans.*, 2018, **47**, 357–366.

56 S. K. Singh, M. F. Beg and G. Rajaraman, Role of Magnetic Exchange Interactions in the Magnetization Relaxation of {3d–4f} Single–Molecule Magnets: A Theoretical Perspective, *Chem. – Eur. J.*, 2016, **22**, 672–680.

57 K. S. Pedersen, G. Lorusso, J. J. Morales, T. Weyhermüller, S. Piligkos, S. K. Singh, D. Larsen, M. Schau-Magnussen, G. Rajaraman and M. Evangelisti, Fluoride–Bridged $\{Gd^{III}_3M^{III}_2\}$ (M = Cr, Fe, Ga) Molecular Magnetic Refrigerants, *Angew. Chem., Int. Ed.*, 2014, **53**, 2394–2397.

58 K. Wade, Ligand field theory and its applications, ed. B. N. Figgis and M. A. Hitchman, Wiley-VCH, New York, 2000, xviii+354, £ 51.95, ISBN 0.471-31776-4, 2000, pp. 449–450.

59 M. E. Lines, Orbital angular momentum in the theory of paramagnetic clusters, *J. Chem. Phys.*, 1971, **55**, 2977–2984.

60 L. Noodleman, Valence bond description of antiferromagnetic coupling in transition metal dimers, *J. Chem. Phys.*, 1981, **74**, 5737–5743.

61 M. J. Frisch, G. W. Trucks, H. B. Schlegel, G. E. Scuseria, M. A. Robb, J. R. Cheeseman, G. Scalmani, V. Barone, G. A. Petersson and H. Nakatsuji, *Gaussian 16 Revision C.*

01, 2016, Gaussian Inc., Wallingford, CT, 2016, vol. **1**, pp. 572.

62 K. R. Vignesh, S. K. Langley, A. Swain, B. Moubaraki, M. Damjanović, W. Wernsdorfer, G. Rajaraman and K. S. Murray, Slow Magnetic Relaxation and Single–Molecule Toroidal Behaviour in a Family of Heptanuclear $\{Cr^{III}Ln^{III}_6\}$ (Ln = Tb, Ho, Er) Complexes, *Angew. Chem., Int. Ed.*, 2018, **57**, 779–784.

63 J. J. Le Roy, L. Ungur, I. Korobkov, L. F. Chibotaru and M. Murugesu, Coupling strategies to enhance single-molecule magnet properties of erbium–cyclooctatetraenyl complexes, *J. Am. Chem. Soc.*, 2014, **136**, 8003–8010.

64 O. Kahn, *Molecular magnetism*, Courier Dover Publications, 2021.

65 G. Rajaraman, F. Totti, A. Bencini, A. Caneschi, R. Sessoli and D. Gatteschi, Density functional studies on the exchange interaction of a dinuclear Gd(III)–Cu(II) complex: method assessment, magnetic coupling mechanism and magneto-structural correlations, *Dalton Trans.*, 2009, 3153–3161.

66 S. K. Singh, N. K. Tibrewal and G. Rajaraman, Density functional studies on dinuclear $\{Ni^{II}Gd^{III}\}$ and trinuclear $\{Ni^{II}Gd^{III}Ni^{II}\}$ complexes: magnetic exchange and magneto-structural maps, *Dalton Trans.*, 2011, **40**, 10897–10906.

67 K. R. Vignesh, S. K. Langley, C. J. Gartshore, I. Borilović, C. M. Forsyth, G. Rajaraman and K. S. Murray, Rationalizing the sign and magnitude of the magnetic coupling and anisotropy in dinuclear manganese(III) complexes, *Dalton Trans.*, 2018, **47**, 11820–11833.

68 K. R. Vignesh, S. K. Langley, K. S. Murray and G. Rajaraman, Exploring the influence of diamagnetic ions on the mechanism of magnetization relaxation in $\{Co^{III}_2Ln^{III}_2\}$ (Ln = Dy, Tb, Ho) "butterfly" complexes, *Inorg. Chem.*, 2017, **56**, 2518–2532.

69 A. Gharu and K. R. Vignesh, Theoretical exploration of single-molecule magnetic and single-molecule toroic behaviors in peroxide-bridged double-triangular $\{M^{II}_3Ln^{III}_3\}$ (M = Ni, Cu and Zn; Ln = Gd, Tb and Dy) complexes, *Dalton Trans.*, 2024, **53**, 13394–13408.

70 D. Schray, D. Westerbeck, J. Braun, Y. Lan, S. Gomez-Coca, W. Wernsdorfer, E. Ruiz, C. E. Anson, J. r. Schnack and A. K. Powell, Fe–Gd Ferromagnetic Cyclic Coordination Cluster $[Fe^{III}_4Gd^{III}_4(teaH)_8(N_3)_8(H_2O)]$ with Magnetic Anisotropy – Theory and Experiment, *Inorg. Chem.*, 2023, **62**, 6642–6648.

71 N. C. Jana, Z. Jagličić, R. Herchel, P. Brandão, R. Nandy and A. Panja, Insight into the Magnetic Exchange Interactions and Anisotropy in Heterobimetallic Cu^{II}–Ln^{III} Complexes: A Rare Example of Cu–Gd Single-Molecule Magnets, *Cryst. Growth Des.*, 2024, **24**, 7537–7548.

72 F. Aquilante, J. Autschbach, R. K. Carlson, L. F. Chibotaru, M. G. Delcey, L. De Vico, N. Ferré, L. M. Frutos, L. Gagliardi and M. Garavelli, Molcas 8: New capabilities for multiconfigurational quantum chemical calculations across the periodic table, *J. Comput. Chem.*, 2016, **37**, 506–541.

73 B. O. Roos and P.-Å. Malmqvist, Relativistic quantum chemistry: the multiconfigurational approach, *Phys. Chem. Chem. Phys.*, 2004, **6**, 2919–2927.

74 B. O. Roos, R. Lindh, P.-Å. Malmqvist, V. Veryazov, P.-O. Widmark and A. C. Borin, New relativistic atomic natural orbital basis sets for lanthanide atoms with applications to the Ce diatom and LuF_3, *J. Phys. Chem. A*, 2008, **112**, 11431–11435.

75 P. Å. Malmqvist, B. O. Roos and B. Schimmelpfennig, The restricted active space (RAS) state interaction approach with spin–orbit coupling, *Chem. Phys. Lett.*, 2002, **357**, 230–240.

76 L. F. Chibotaru and L. Ungur, *Ab initio* calculation of anisotropic magnetic properties of complexes. I. Unique definition of pseudospin Hamiltonians and their derivation, *J. Chem. Phys.*, 2012, **137**, 064112.

77 A. D. Becke, Density–functional thermochemistry. III. The role of exact exchange, *J. Chem. Phys.*, 1993, **98**, 5648–5652.

78 T. R. Cundari and W. J. Stevens, Effective core potential methods for the lanthanides, *J. Chem. Phys.*, 1993, **98**, 5555–5565.

79 (*a*) CCDC 2456392: Experimental Crystal Structure Determination, 2025, DOI: **10.5517/ccdc.csd.cc2ng2gp**; (*b*) CCDC 2456393: Experimental Crystal Structure Determination, 2025, DOI: **10.5517/ccdc.csd.cc2ng2hq**; (*c*) CCDC 2456394: Experimental Crystal Structure Determination, 2025, DOI: **10.5517/ccdc.csd.cc2ng2jr**.